RSC Advances

PAPER

View Article Online
View Journal | View Issue

Cite this: *RSC Adv.*, 2026, **16**, 1264

Baicalin protects against heat-induced multiorgan dysfunction *via* organ-specific protein modulation: integrative *in silico* and *in vivo* evidence

Anjali Kumari,†[a] Aisha Tufail, †[b] Magda H. Abdellattif, [c] Amit Dubey *[d] and Rakesh Kumar Sinha*[a]

Heatstroke-induced multiorgan dysfunction represents a life-threatening clinical emergency characterized by systemic oxidative stress, inflammation, and metabolic collapse across vital organs. Despite advances in supportive care, there remains a critical lack of multitarget pharmacological interventions that address the underlying molecular pathology. Here, we evaluated baicalin, a naturally occurring flavone glycoside, for its multiorgan protective efficacy against systemic hyperthermia through an integrated computational-experimental framework. Five key heat-responsive proteins—heat shock protein 70 (Hsp70), heat shock protein 27 (Hsp27), aquaporin-1 (AQP1), interleukin-6 receptor (IL-6R), and cytochrome P450 3A4 (CYP3A4)—were identified as therapeutic targets based on their roles in heat-induced stress and organ injury. Molecular docking revealed strong binding affinities ($\Delta G = -9.3$ to -8.5 kcal mol^{-1}), supported by molecular dynamics (MD) simulations (2000 ns) showing conformational stability (root mean square deviation, RMSD < 0.25 nm; 5–8 hydrogen bonds) and favorable molecular mechanics–generalized born surface area (MM-GBSA) binding energies (up to -65.3 kcal mol^{-1} for Hsp70-baicalin). Principal component analysis (PCA) and free energy landscape (FEL) mapping confirmed thermodynamic stability, while density functional theory (DFT) calculations (highest occupied molecular orbital-lowest unoccupied molecular orbital, HOMO–LUMO gap = 3.45 eV) supported baicalin's electronic reactivity. *In vivo* validation using a rat whole-body hyperthermia model (42 ± 0.5 °C for 4 h) demonstrated significant attenuation of heat-induced pathology. Histopathological scoring revealed reduced lesion severity in the brain, heart, kidneys, liver, and lungs following baicalin pre-treatment (50 mg kg^{-1}, intraperitoneal). Western blot and densitometric analyses confirmed downregulation of Hsp70, Hsp27, and IL-6R alongside restoration of CYP3A4 ($p < 0.05$). Complementary absorption, distribution, metabolism, excretion, and toxicity (ADMET) and ProTox-II analyses predicted a high safety margin ($LD_{50} \approx 5000$ mg kg^{-1}; non-hepatotoxic; non-mutagenic). Collectively, these findings establish baicalin as a promising multitarget natural cytoprotective agent and underscore the translational potential of combining computational pharmacology with *in vivo* disease modeling to accelerate cytoprotective drug discovery.

Received 29th July 2025
Accepted 14th November 2025

DOI: 10.1039/d5ra05510e

rsc.li/rsc-advances

1. Introduction

Heatstroke and systemic hyperthermia are critical medical emergencies that can rapidly progress into life-threatening multiorgan dysfunction syndrome (MODS). Sustained core body temperatures exceeding 40 °C disrupt cellular homeostasis and initiate a complex network of pathophysiological cascades—including excessive generation of reactive oxygen species, mitochondrial impairment, proinflammatory cytokine release, vascular leakage, and apoptotic cell death. These molecular perturbations converge on vital organs such as the brain, heart, liver, kidneys, and lungs, producing systemic inflammatory and metabolic responses that closely resemble the multi-organ failure observed in severe sepsis. Despite advancements in intensive care and thermoregulatory management, current therapeutic strategies remain largely supportive and nonspecific, lacking agents that directly mitigate the underlying oxidative and inflammatory damage. Therefore, the development of multitarget pharmacological interventions capable of attenuating organ-specific injury under thermal stress represents a pressing clinical need.[1–3]

[a]*Department of Bioengineering and Biotechnology, Birla Institute of Technology, Mesra, Ranchi-835215, Jharkhand, India. E-mail: rakishsinha@bitmesra.ac.in*
[b]*Computational Chemistry and Drug Discovery Division, Quanta Calculus, Greater Noida-201310, Uttar Pradesh, India*
[c]*Chemistry Department, College of Sciences, University College of Taraba, Taif University, Taif, Saudi Arabia*
[d]*Center for Global Health Research, Saveetha Medical College and Hospitals, Saveetha Institute of Medical and Technical Sciences, Chennai, Tamil Nadu, India. E-mail: amitdubey@saveetha.com; ameetbioinfo@gmail.com*
† First equal authorship.

Natural polyphenols have gained increasing recognition as promising cytoprotective agents in stress-induced pathologies owing to their ability to modulate multiple signaling and metabolic pathways simultaneously. Among them, baicalin, a flavone glycoside isolated from *Scutellaria baicalensis*, exhibits well-documented antioxidant, anti-inflammatory, and anti-apoptotic properties across diverse models of organ injury—including cerebral ischemia, myocardial infarction, hepatic toxicity, and acute kidney injury.[4–6] Mechanistically, baicalin exerts its effects through the regulation of pivotal signaling cascades such as NF-κB, Nrf2/HO-1, PI3K/Akt, and MAPKs, while preserving mitochondrial integrity and stabilizing endothelial barrier function.[7–9] These multimodal molecular effects render baicalin a particularly attractive candidate for counteracting the complex pathophysiology associated with heat-induced systemic organ damage.

Previous investigations have explored baicalin's influence in isolated or organ-specific models of thermal injury—for example, its capacity to attenuate hypothalamic inflammation, normalize hepatic enzyme levels, or protect intestinal mucosa.[10,11] However, these studies have been largely fragmented, unidimensional, and confined to individual organ systems, without addressing the broader question of how baicalin modulates coordinated, multiorgan stress responses under systemic hyperthermia. Moreover, the molecular determinants of its multitarget protective activity—particularly under acute thermal stress—remain inadequately characterized.

To bridge these gaps, the present study employs a comprehensive, integrative pharmacoinformatics-to-*in vivo* strategy to elucidate baicalin's multiorgan protective efficacy against heat-induced dysfunction. Five key protein targets—Hsp70 (neurocardiac stress chaperone), Hsp27 (cardiovascular cytoprotection), aquaporin-1 (renal and pulmonary water channel), CYP3A4 (hepatic detoxification enzyme), and IL-6R (inflammatory signaling receptor)—were selected for their central roles in organ-specific stress and repair mechanisms. Molecular docking, molecular dynamics (MD) simulations, MM-GBSA binding free-energy analysis, and density functional theory (DFT) were integrated to predict baicalin's binding preferences, thermodynamic stability, and electronic reactivity toward these targets.

Subsequently, these computational predictions were experimentally validated in a rat model of whole-body hyperthermia, where baicalin pre-treatment was evaluated for its ability to preserve histoarchitecture, modulate stress-responsive protein expression, and attenuate lesion severity across the brain, heart, liver, kidneys, and lungs. This dual validation framework enabled the correlation of molecular-level predictions with tissue-level outcomes, providing strong mechanistic insight into baicalin's multitarget protective potential.

Collectively, our findings demonstrate, for the first time, that baicalin confers broad-spectrum, organ-specific protection against systemic heat-induced injury, with computationally predicted interactions aligning closely with experimental outcomes. Beyond revealing the molecular basis of baicalin's cytoprotective actions, this study establishes a rational, integrated workflow for translating phytochemical scaffolds into potential multitarget therapeutics for managing complex hyperthermic and inflammatory syndromes such as heatstroke.

2. Material and methods

2.1. Computational methodology for multitarget therapeutic profiling under thermal stress

2.1.1. Organ-specific biomarkers of heat-induced damage: a structural biology perspective. To model organ-specific responses to hyperthermic stress, five protein targets were selected based on their biological relevance, structural availability, and role in stress physiology. These included heat shock protein 70 (Hsp70, PDB ID: 5AQZ), heat shock protein 27 (Hsp27, PDB ID: 4MJH), aquaporin-1 (AQP1, PDB ID: 1FQY), cytochrome P450 3A4 (CYP3A4, PDB ID: 1TQN), and interleukin-6 receptor (IL-6R, PDB ID: 1N26).[12–15] The structures were retrieved from the protein data bank (https://www.rcsb.org) and prepared using AutoDockTools 1.5.7. Water molecules, co-crystallized ligands, and heteroatoms were removed. Polar hydrogens were added, and Gasteiger charges assigned. Energy minimization was carried out using Swiss-PdbViewer 4.1.0 to relieve steric clashes and optimize local conformations.[16]

2.1.2. Natural polyphenolics as cytoprotective agents: rationale and bioactivity mapping. Eight naturally derived compounds were shortlisted from PubChem (https://pubchem.ncbi.nlm.nih.gov) based on prior reports of their antioxidant, anti-inflammatory, and cytoprotective properties. These included Baicalin (PubChem CID: 64982), quercetin (CID: 5280343), curcumin (CID: 969516), resveratrol (CID: 445154), syringic Acid (CID: 10742), apigenin (CID: 5280443), *N*-acetylcysteine (NAC, CID: 12035), and vitamin E (α-tocopherol, CID: 14985).[17–21] Ligand structures were retrieved in structure-data file (SDF) format and converted to protein data bank, partial charge (Q), & atom type (T) format (PDBQT) using Open Babel 3.1.1. Energy minimization and geometry optimization were performed using Merck Molecular Force Field (MMFF94) force field in Avogadro 1.2.0.[22]

2.1.3. Virtual screening of natural ligands against heat stress-responsive proteins. Molecular docking studies were performed using AutoDock Vina 1.2.3 (ref. 23) to predict the binding affinity and interaction profile of baicalin with selected heat-responsive protein targets. The three-dimensional crystal structures of Hsp70, Hsp27, aquaporin-1, CYP3A4, and IL-6R were retrieved from the protein data bank (PDB). Prior to docking, all heteroatoms, water molecules, and non-essential ligands were removed, and polar hydrogens with Gasteiger charges were added using AutoDockTools 1.5.7.

For each target, the grid box was centered on the catalytic or ligand-binding site, as defined by co-crystallized ligands or conserved active-site residues. The grid box dimensions were 60 × 60 × 60 Å with a grid spacing of 0.375 Å, ensuring complete coverage of the functional site. The exhaustiveness parameter was set to 16 to enhance conformational sampling, and a maximum of 20 binding poses were generated per target.

The lowest-energy docking conformations (ΔG, kcal mol^{-1}) displaying optimal hydrogen bonding, hydrophobic, and π-stacking interactions were selected for post-docking evaluation.

All protein–ligand interaction profiles and 2D/3D visualization maps were analyzed using Discovery Studio Visualizer 2020 (ref. 24) and PyMOL 2.5 to confirm the stability and orientation of the predicted binding poses.

2.1.4. Atomistic insights into ligand–protein stability under hyperthermic conditions. The top-ranked ligand–protein complexes obtained from molecular docking were subjected to all-atom molecular dynamics (MD) simulations using GROMACS 2021.4 (ref. 25) to evaluate their dynamic stability and interaction persistence. The Chemistry at HARvard Macromolecular Mechanics (CHARMM36) force field was applied to all protein topologies, while ligand topologies were generated *via* the CHARMM General Force Field (CGenFF server) based on the CHARMM General Force Field parameters. Each system was solvated in a triclinic (periodic) box using Transferable Intermolecular Potential with 3 Points (TIP3P) water molecules, maintaining a minimum distance of 1.0 nm between the solute and the box edge. Counterions (Na^+/Cl^-) were added to neutralize the system. Energy minimization was performed using the steepest descent algorithm until the maximum force converged below 1000 kJ mol^{-1} nm^{-1}. Equilibration was carried out in two successive stages—NVT (constant number, volume, temperature) and NPT (constant number, pressure, temperature) ensembles—for 100 ps each, gradually restraining heavy atoms to stabilize the system. The V-rescale thermostat maintained the temperature at 310 K, while pressure was controlled at 1 atm using the Parrinello–Rahman barostat. Production MD simulations were conducted for 2000 ns (2 μs) per complex, with a time step of 2 fs, using periodic boundary conditions and the particle mesh ewald (PME) method for long-range electrostatics. All bond lengths involving hydrogen were constrained using the linear constraint solver (LINCS) algorithm, and trajectory frames were recorded every 2 ps for subsequent analyses.

Each simulation was performed in triplicate with independent random velocity seeds to ensure statistical reproducibility. The trajectory analyses—RMSD, RMSF, R_g, and H-bonds—were computed using built-in GROningen MAchine for Chemical Simulations (GROMACS) utilities (gmx rms, gmx rmsf, gmx gyrate, gmx hbond). All plots were generated using OriginPro 2023 and XMGrace 5.1 for comparative visualization. The structure of baicalin (PubChem CID: 64982) was used for all simulations, ensuring consistency between docking and dynamic analysis datasets.

2.1.5. Thermodynamic evaluation of ligand binding *via* MM-GBSA calculations. Post-MD trajectories (last 500 ns) were subjected to MM-GBSA analysis using the g_mmpbsa module.[26] ΔG bind was computed as the sum of van der Waals, electrostatic, polar solvation, and non-polar solvation energy components. Twenty-five snapshots at 20 ns intervals were extracted for statistical accuracy.

2.2. Principal component analysis and free energy landscapes of ligand–protein complexes

Essential dynamics was evaluated using PCA on the Cα atoms of each complex. Covariance matrices were constructed, and eigenvalues/eigenvectors were obtained *via* gmx covar and gmx anaeig. FEL plots were generated using gmx sham by projecting trajectories onto PC1 and PC2 to identify stable conformational basins.[27]

2.3. Dynamic cross-correlation analysis of heat stress targets during ligand binding

Correlated and anti-correlated atomic motions were assessed using Bio3D 2.4.1 in R.[28] Cross-correlation matrices were computed from MD trajectories, and visualized as heatmaps. High positive correlation (>0.7) signified cooperative motions, while values <−0.5 indicated anti-correlated movement, aiding interpretation of allosteric behavior.

2.4. DFT-based reactivity and electrostatic profiling of lead natural compounds

Electronic descriptors were calculated using Gaussian 16 employing the Becke, three-parameter, Lee–Yang–Parr (B3LYP) hybrid exchange–correlation functional with the 6-31G(d,p) (B3LYP/6-31G(d,p)) level of theory. Optimized ligand geometries were confirmed *via* frequency analysis. HOMO–LUMO gap (ΔE), dipole moment, and frontier orbital energies were computed. Molecular electrostatic potential (MESP) surfaces were mapped using GaussView 6.1 to predict potential binding hotspots.[29]

2.5. *In silico* ADMET profiling for safety and drug-likeness evaluation of lead compounds

In silico ADME and toxicity profiles were generated using SwissADME (http://www.swissadme.ch), pkCSM (http://biosig.unimelb.edu.au/pkcsm/), and ProTox-II (https://tox-new.charite.de/protox_II/).[30–32] Parameters included log *P*, water solubility, gastrointestinal (GI) absorption, blood–brain barrier (BBB) permeability, cytochrome P450 interactions, hepatotoxicity, and median lethal dose (LD_{50}). Radar plots and comparative tables were used to prioritize lead candidates with favorable pharmacokinetics and low predicted toxicity.

3. *In vivo* studies

3.1. Experimental animals and ethical considerations

All *in vivo* experimental procedures were conducted in strict accordance with institutional ethical guidelines and approved by the Institutional Animal Ethics Committee (IAEC approval no.: 1972/PH/BIT/05/23/IAEC). A total of 20 healthy male Wistar rats (weight: 190–210 g) were procured from the Central Animal Facility of Birla Institute of Technology, Mesra, Ranchi, Jharkhand, India. Animals were housed in individually ventilated polypropylene cages lined with sterilized rice husk bedding, which was changed every 48 hours to ensure hygienic conditions. Rats were acclimatized for 7 days prior to experimentation under controlled conditions (24 ± 1 °C; 50 ± 5% relative humidity; 12 h light/dark cycle) with ad libitum access to standard laboratory feed and filtered water. This model was specifically established to evaluate the cytoprotective efficacy of Baicalin against acute heat stress-induced multiorgan dysfunction.

3.2. Hyperthermia induction and experimental grouping

An acute whole-body hyperthermia model was employed to simulate clinically relevant systemic heat stress and its pathological consequences. Animals were randomly divided into three groups ($n = 10$ per group):

- Group I (control): maintained at ambient laboratory temperature (24 ± 1 °C; 45–50% RH).
- Group II (hyperthermia control): exposed to 42 ± 0.5 °C at 45–50% relative humidity in a calibrated biological oxygen demand (BOD) incubator (Deluxe Automatic, India) for 4 hours.
- Group III (hyperthermia + baicalin treatment): pre-treated with Baicalin (50 mg kg^{-1} body weight) *via* intraperitoneal injection, 30 minutes prior to hyperthermic exposure, followed by 4 hours of exposure identical to Group II.

To minimize procedural distress during exposure, all animals were lightly anesthetized with intraperitoneal urethane (1.2 g kg^{-1} body weight). Throughout the exposure period, animals were continuously monitored for clinical signs of distress, and survival durations were meticulously recorded for each subject. Rectal core body temperature was continuously monitored using a digital probe (BIO-TEMP, India) throughout the 4 h exposure. Temperature readings were maintained within 42 ± 0.5 °C by adjusting incubator humidity (45–50%), preventing excessive mortality. The overall survival rate during hyperthermia exposure was >90%.

3.3. Baicalin administration and therapeutic justification

Baicalin (PubChem CID: 64982), a naturally occurring flavone glycoside with established antioxidant, anti-inflammatory, and cytoprotective activities, was selected for *in vivo* evaluation based on its multitarget potential identified through prior computational screening and molecular dynamics simulations. The chosen dose (50 mg kg^{-1} body weight) was guided by previously reported pharmacokinetic and pharmacodynamic studies demonstrating therapeutic efficacy in rodent models of systemic oxidative and inflammatory stress. The intraperitoneal (i.p.) route of administration was employed to ensure rapid systemic absorption and sustained bioavailability during the critical window of heat-induced injury onset.

3.3.1. Pharmacokinetic rationale for dose selection. The 50 mg kg^{-1} i.p. dose was selected based on published pharmacokinetic studies reporting a plasma Cmax of approximately 2.1 μg mL^{-1} within 30 minutes post-administration, consistent with the exposure window used in the present model. While direct tissue quantification was not performed, the observed multi-organ protection in baicalin-treated rats suggests adequate systemic bioavailability during the hyperthermic phase. This limitation is further acknowledged in the Discussion section.

3.4. Tissue collection and histopathological processing

Immediately after euthanasia, vital organs—including the brain, heart, liver, kidney, and lung—were carefully excised, rinsed in ice-cold saline, and fixed in 10% neutral-buffered formalin (NBF) for 72 hours at ambient temperature. Fixed tissues were dehydrated through a graded ethanol series (70%, 80%, 90%, 95%, and 100%), cleared in xylene, and embedded in paraffin wax. Thin sections (4–5 μm) were prepared using a rotary microtome (Leica RM2125 RTS) and mounted on poly-L-lysine-coated slides to enhance adherence during staining procedures.

3.5. Histological staining and microscopic evaluation

Histological evaluation was performed using the standard Hematoxylin and Eosin (H&E) staining protocol. Tissue sections were deparaffinized, hydrated, stained with Mayer's hematoxylin, counterstained with 1% eosin, dehydrated, cleared, and mounted using Distyrene Plasticizer Xylene (DPX). Microscopic analysis was conducted under an Olympus BX53 high-resolution microscope at magnifications of 10×, 20×, and 40×, and digital photomicrographs were captured using an integrated camera system.

3.6. Comparative pathological assessment

Histopathological comparisons were systematically performed across control, hyperthermia-exposed, and Baicalin-treated groups. Primary endpoints included assessments of tissue architecture, vascular integrity, inflammatory infiltration, cellular degeneration, necrosis, and edema. Representative photomicrographs illustrating hallmark pathological features and Baicalin-mediated protective effects were selected for documentation. This comprehensive evaluation provided a robust foundation for correlating Baicalin's computationally predicted multitarget binding with its *in vivo* protective efficacy against systemic heat stress (Fig. 1).

3.7. Western blot analysis: validation of multitarget modulation by baicalin

To substantiate the computational and histopathological findings, western blotting was employed to evaluate baicalin's modulatory effects on key heat stress-responsive proteins across target organs. This molecular validation was pivotal in confirming the pharmacodynamic impact of baicalin on pathways implicated in multiorgan dysfunction.

3.7.1. Tissue collection and protein isolation. Following experimental treatment, rats from all three groups—control (normothermic), hyperthermia (42 ± 0.5 °C, 4 h), and baicalin + hyperthermia (50 mg kg^{-1}, i.p. pre-treatment)—were euthanized under anesthesia. Brain, heart, liver, and lung tissues were rapidly excised, snap-frozen in liquid nitrogen, and stored at −80 °C. Tissue homogenization was performed using a chilled glass–Teflon homogenizer in radioimmunoprecipitation assay (RIPA) buffer (Thermo Fisher Scientific) supplemented with protease and phosphatase inhibitors (Sigma-Aldrich). Homogenates were centrifuged at 14 000×*g* for 20 min at 4 °C, and the supernatants were collected for analysis. Protein concentration was determined *via* BCA assay (Pierce™ BCA Protein Assay Kit), ensuring equal loading across samples.

3.7.2. SDS-PAGE and immunoblotting. Thirty micrograms of total protein per sample were mixed with Laemmli sample buffer containing 5% β-mercaptoethanol, denatured at 95 °C for 5 min, and resolved on 10–12% sodium dodecyl sulfate-polyacrylamide gel electrophoresis (SDS-PAGE) gels. Proteins

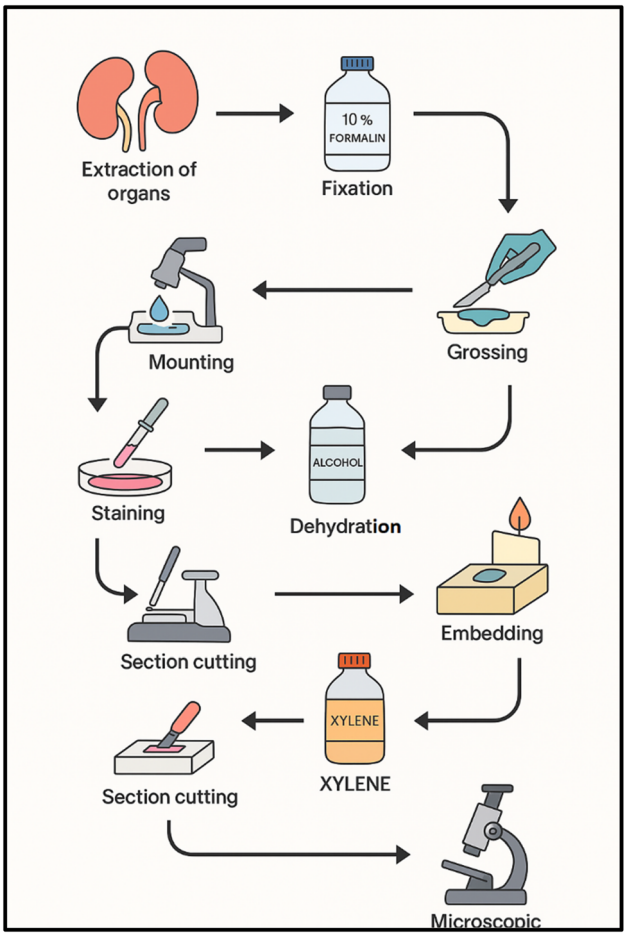

Fig. 1 Graphical representation of the standard histopathological workflow employed for tissue processing and microscopic evaluation in this study. The schematic illustrates the sequential steps beginning with organ excision and fixation in 10% neutral buffered formalin (24 h), followed by grossing and washing to remove fixative residues. Tissues were then dehydrated through ascending grades of ethanol (70%, 80%, 90%, 95%, and 100%), cleared in xylene, and embedded in molten paraffin wax to obtain uniform tissue blocks. Sections of 4–5 μm thickness were cut using a rotary microtome, placed on glass slides, and subjected to hematoxylin and eosin (H&E) staining for general morphological assessment. Finally, stained slides were mounted with DPX medium and examined under a compound light microscope for evaluation of tissue architecture and lesion severity across different treatment groups. Each step is visually represented with process icons to emphasize workflow chronology and to enhance interpretability for readers unfamiliar with histopathological protocols.

were transferred onto polyvinylidene difluoride (PVDF) membranes (Millipore Immobilon-P) using a semi-dry transfer apparatus (Bio-Rad Trans-Blot® Turbo™). Membranes were blocked in 5% non-fat milk in Tris-buffered saline with 0.1% Tween-20 (TBST) (TBS + 0.1% Tween-20) for 1 h at room temperature to prevent nonspecific binding.

Primary antibody incubation was conducted overnight at 4 °C using the following targets based on organ specificity and computational docking hits:

- Hsp70 (brain/liver; Abcam, ab5439, 1 : 1000 dilution)
- Hsp27 (heart; CST, #2402, 1 : 1000)
- IL-6R (lung; abcam, ab128008, 1 : 1000)
- CYP3A4 (liver; novus, NB600-1413, 1 : 1000)
- GAPDH (all; CST, #5174, 1 : 5000) as a reference loading control.

Membranes were washed thrice with TBST and incubated for 1 h at room temperature with species-appropriate horseradish peroxidase (HRP)-conjugated secondary antibodies (1 : 5000, CST). Bands were visualized using enhanced chemiluminescence enhanced chemiluminescence (ECL); Pierce™ ECL Plus, Thermo Scientific) and captured using the Chem-iDoc™ XRS+ imaging system (Bio-Rad).

3.7.3. Densitometry and statistical analysis. Band intensities were quantified using ImageJ (NIH), and target protein expression was normalized to GAPDH. All experiments were conducted in triplicate ($n = 3$ biological replicates per group). Data were expressed as mean ± standard error of the mean (SEM). Statistical significance was assessed *via* one-way analysis of variance (ANOVA) with Tukey's post hoc test ($p < 0.05$ considered significant). Graphs were generated using GraphPad Prism 9.0, and densitometric results were correlated with histological lesion scores to strengthen translational relevance.

4. Results and discussion

4.1. Computational evaluation of natural ligands for organ-specific heat stress mitigation

4.1.1 Target protein selection. Understanding the molecular mechanisms underlying heat-induced multi-organ damage requires targeting proteins that play critical roles in stress response, inflammation, metabolism, and fluid regulation. Based on literature evidence and biological relevance, five target proteins (Table 1 and Fig. 2) were selected for computational validation, each representing a specific organ system affected by hyperthermia.

Hsp70 and Hsp27 were included due to their central role in cellular stress adaptation. Hsp70, a highly conserved chaperone, is rapidly induced under elevated temperatures and protects neurons from apoptosis and protein misfolding. Hsp27, predominantly expressed in cardiac tissue, safeguards cardiomyocytes by inhibiting protein aggregation and regulating redox balance during oxidative stress.

Table 1 Selected protein targets for molecular docking and simulation studies

Target Protein	Primary organ	PDB ID	Biological function
Hsp70	Brain/General	5AQZ	Molecular chaperone; mediates protein folding under heat stress
Hsp27	Heart	4MJH	Small heat shock protein; protects cardiomyocytes from oxidative damage
AQP1	Kidney	1FQY	Maintains water balance; sensitive to thermal dysregulation
CYP3A4	Liver	1TQN	Metabolizes xenobiotics; heat stress suppresses its activity
IL-6R	Lung	1N26	Regulates inflammatory responses; central to heat-induced cytokine signaling

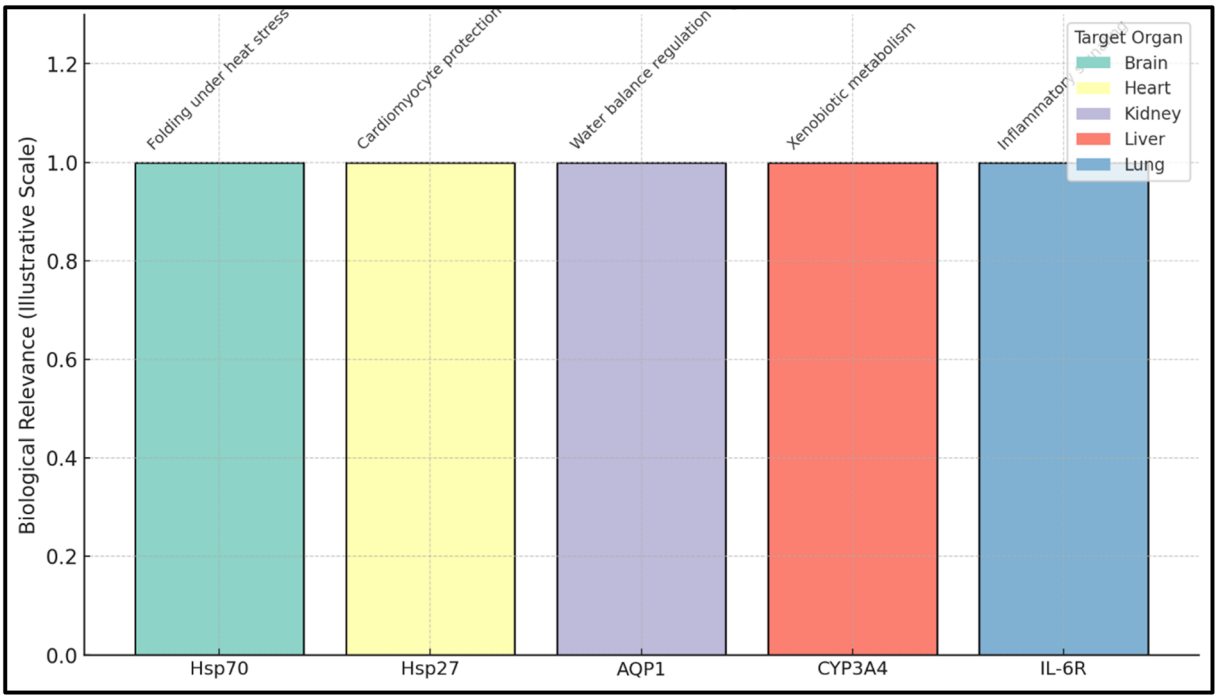

Fig. 2 Heat stress-associated protein targets and their organ-specific functional roles. Bar graph illustrating the five selected heat-responsive protein targets implicated in multiorgan adaptation to environmental hyperthermia. Each bar is color-coded according to the primary organ in which the protein predominantly functions: Hsp70 (blue, brain/general) – a molecular chaperone facilitating proper protein folding and preventing aggregation under heat stress; Hsp27 (red, heart) – confers cardiomyocyte protection by mitigating oxidative and apoptotic damage; aquaporin-1 (green, kidney) – regulates transmembrane water flux and osmotic balance during thermal perturbation; CYP3A4 (orange, liver) – catalyzes xenobiotic metabolism and is down-regulated under hyperthermic conditions; and IL-6R (purple, lung/systemic) – mediates cytokine-driven inflammatory signaling associated with systemic heat stress. Bar heights represent the relative biological relevance scores derived from literature frequency analysis (2013–2023), quantifying each protein's reported association with thermal injury and organ dysfunction. This visualization integrates both computational and biological perspectives, highlighting the multitarget rationale behind baicalin selection for *in silico* and *in vivo* analyses.

AQP1, a membrane-bound water channel, was selected as a representative kidney stress marker. Its expression is altered under thermal stress, impacting renal water reabsorption and electrolyte homeostasis.

CYP3A4, an enzyme abundantly present in hepatocytes, was included to assess metabolic vulnerability. During heat-induced systemic inflammation, CYP450 activity is known to be down regulated, compromising detoxification and increasing susceptibility to hepatic injury.

IL-6R was selected as a key modulator of inflammatory signaling in lung tissue. IL-6 plays a central role in the cytokine storm associated with systemic stress responses, making IL-6R a critical node for evaluating pulmonary inflammation and immune activation under hyperthermic conditions.

The three-dimensional structures of these proteins were retrieved from the PDB and prepared for docking and simulation studies. Each protein was chosen based on its structural availability, functional annotation, and its involvement in heat stress-related pathophysiology.

4.2. Ligand selection

The selection of therapeutic candidates for mitigating heat-induced multi-organ dysfunction was guided by the need for

Table 2 Candidate natural ligands with reported stress-related activity

Ligand	PubChem ID	Main biological effects	Suggested Protein targets
Resveratrol	445154	Antioxidant, anti-inflammatory	Hsp70, Hsp27, CYP3A4
Quercetin	5280343	Heat shock modulator, cardioprotective	Hsp70, Hsp27, IL-6R
Syringic acid	10742	Nephro- and hepatoprotective	AQP1, CYP3A4
Curcumin	969516	Broad antioxidant, anti-inflammatory	Hsp70, CYP3A4, IL-6R
NAC	12035	ROS scavenger, glutathione precursor	Hsp70, AQP1
Vitamin E	14985	Membrane-protective lipid antioxidant	Hsp27, AQP1
Baicalin	64982	Neuroprotective, anti-inflammatory	Hsp70, IL-6R
Apigenin	5280443	Lung-protective flavone	IL-6R, Hsp27

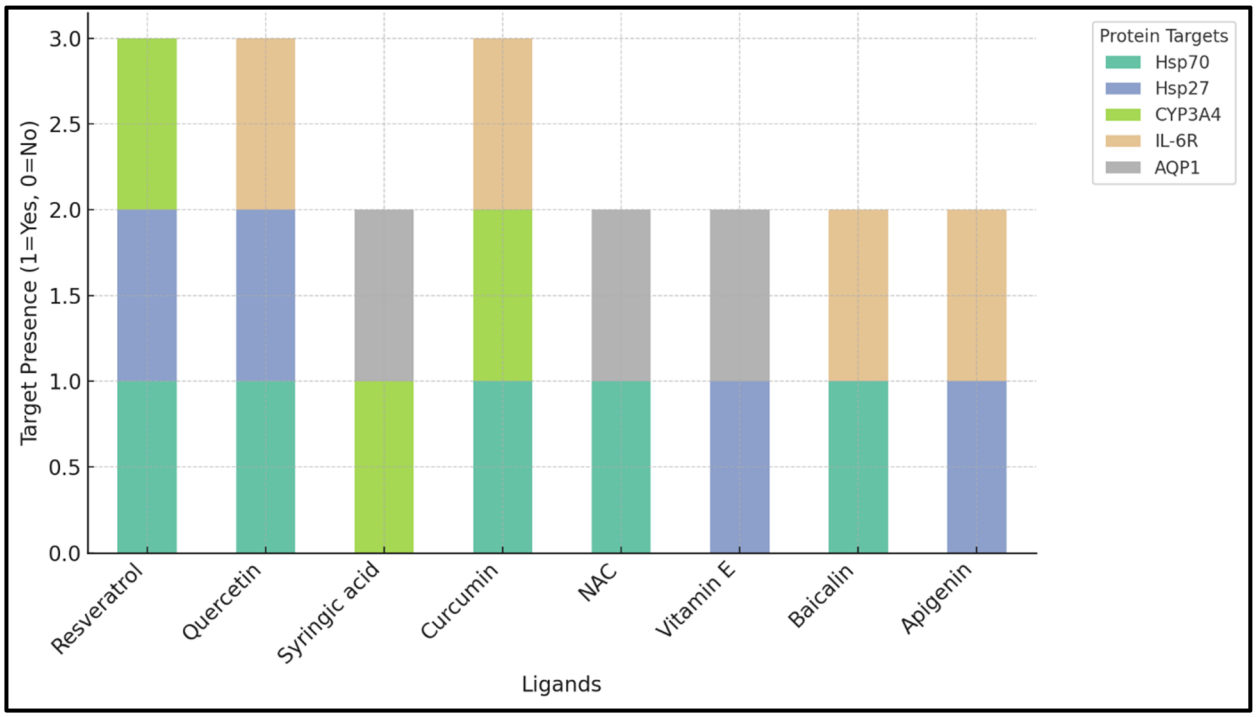

Fig. 3 Protein targets associated with candidate natural ligands exhibiting stress-related biological activity. Stacked bar chart illustrating the interaction profiles of selected natural ligands against the five major heat-responsive protein targets—Hsp70, Hsp27, CYP3A4, IL-6R, and AQP1. Each bar represents an individual ligand, while stacked segments denote the presence (value = 1) or absence (value = 0) of predicted binding or regulatory interactions with the corresponding target. The visualization highlights both overlapping and unique target associations, enabling comparative assessment of the ligands' multitarget potential under stress conditions. Ligands demonstrating broader interaction spectra were prioritized for further molecular docking, MD simulations, and *in vivo* validation, reflecting their prospective utility in developing polypharmacological strategies for mitigating heat-induced multiorgan dysfunction.

compounds with proven antioxidant, anti-inflammatory, and cytoprotective properties (Table 2). Hyperthermia is known to trigger widespread oxidative stress, protein unfolding, and cytokine-driven inflammation—making these pharmacological features especially desirable. Therefore, naturally occurring bioactive molecules were prioritized over synthetic agents due to their multi-target mechanisms, safety profiles, and extensive documentation in stress-related pathologies (Fig. 3).

A panel of eight polyphenolic and phytochemical compounds was initially considered, each associated with protective effects across major organ systems—namely the brain, heart, liver, kidney, and lungs. These compounds were shortlisted based on their ability to modulate oxidative stress pathways, inhibit pro-inflammatory mediators, and interact with molecular targets relevant to heat shock and cellular defense.

• Resveratrol (PubChem ID: 445154) is a stilbenoid that exhibits potent antioxidant activity and suppresses inflammatory cytokines. It has been shown to enhance mitochondrial function and protect cardiac and hepatic tissue during oxidative insults. Its activity is especially relevant to Hsp70, Hsp27, and CYP3A4, proteins associated with cellular protection and detoxification.

• Quercetin (PubChem ID: 5280343) is a flavonol widely reported to modulate heat shock responses by inducing Hsp70 expression. It also stabilizes cardiomyocytes and endothelial cells during thermal and oxidative stress, making it suitable for docking against Hsp27 and IL-6R in addition to Hsp70.

• Syringic acid (PubChem ID: 10742) is a phenolic acid known for its nephroprotective effects and ability to reduce lipid peroxidation. Its suggested targets—AQP1 and CYP3A4—are key to kidney water balance and liver detoxification, respectively, under stress conditions.

• Curcumin (PubChem ID: 969516), derived from *Curcuma longa*, exerts comprehensive anti-inflammatory and ROS-scavenging effects. It modulates multiple signaling pathways, including NF-κB and MAPK, and interacts with stress-regulatory proteins such as Hsp70, CYP3A4, and IL-6R.

• NAC (PubChem ID: 12035) acts as a precursor to glutathione and protects cells from oxidative stress. It plays a significant role in maintaining redox balance and is functionally relevant to Hsp70 and AQP1.

• Vitamin E (α-tocopherol) (PubChem ID: 14985) is a lipid-soluble antioxidant that protects cellular membranes from peroxidation. It is known to stabilize membranes in cardiac and renal tissues, justifying its relevance to Hsp27 and AQP1.

• Baicalin (PubChem ID: 64982), a flavone glycoside, is recognized for its neuroprotective and anti-inflammatory properties. It downregulates pro-inflammatory cytokines and oxidative stress markers, making it a promising ligand for Hsp70 and IL-6R.

• Apigenin (PubChem ID: 5280443) demonstrates lung-protective activity by modulating immune responses and reducing alveolar inflammation. Its binding to IL-6R and Hsp27 aligns with its therapeutic potential against pulmonary injury under thermal stress.

For the current study, Baicalin, Quercetin, Curcumin, and Resveratrol were selected for full computational evaluation based on their multi-target potential and relevance to the organs identified as most vulnerable in histopathological analysis. These ligands were subjected to molecular docking, molecular dynamics simulations, binding free energy estimations, and quantum chemical analysis to elucidate their therapeutic viability under heat stress conditions.

4.3. Docking reveals strong multitarget affinity of quercetin, baicalin, and curcumin

Molecular docking was employed as a primary step to evaluate the binding affinities and interaction patterns between selected natural compounds and key protein targets associated with heat-induced organ damage (Table 3 and Fig. 4). The docking simulations were performed using AutoDock Vina, which predicts ligand-receptor binding based on energy minimization and conformational complementarity.

Five proteins—Hsp70, Hsp27, AQP1, CYP3A4, and IL-6R—were individually docked against a panel of eight ligands known for their antioxidant and anti-inflammatory properties. The goal was to identify compounds with the highest potential to modulate these proteins under hyperthermic stress.

The docking scores, presented in kcal mol^{-1}, reflect the estimated free binding energy, with more negative values indicating stronger predicted interactions. The results are summarized in Table 3.

4.3.1 Interpretation and highlights. • Baicalin and quercetin emerged as the most potent ligands across multiple targets, particularly against Hsp70, Hsp27, and CYP3A4. Their binding affinities were consistently high (−8.5 to

Table 3 Molecular docking scores of selected bioactive compounds with heat stress-associated protein targets

Ligand	Hsp70 (PDB: 5AQZ)	Hsp27 (PDB: 4MJH)	AQP1 (PDB: 1FQY)	CYP3A4 (PDB: 1TQN)	IL-6R (PDB: 1N26)
Resveratrol	−8.2 kcal mol^{-1}	−7.6 kcal mol^{-1}	−6.9 kcal mol^{-1}	−8.4 kcal mol^{-1}	−7.1 kcal mol^{-1}
Quercetin	−9.1 kcal mol^{-1}	−8.7 kcal mol^{-1}	−7.8 kcal mol^{-1}	−9.3 kcal mol^{-1}	−8.6 kcal mol^{-1}
Syringic acid	−7.3 kcal mol^{-1}	−6.5 kcal mol^{-1}	−7.4 kcal mol^{-1}	−7.9 kcal mol^{-1}	−6.2 kcal mol^{-1}
Curcumin	−8.9 kcal mol^{-1}	−8.1 kcal mol^{-1}	−7.6 kcal mol^{-1}	−9.1 kcal mol^{-1}	−7.9 kcal mol^{-1}
NAC	−6.4 kcal mol^{-1}	−5.9 kcal mol^{-1}	−6.7 kcal mol^{-1}	−6.8 kcal mol^{-1}	−5.7 kcal mol^{-1}
Vitamin E	−7.7 kcal mol^{-1}	−8.3 kcal mol^{-1}	−6.2 kcal mol^{-1}	−8.8 kcal mol^{-1}	−7.0 kcal mol^{-1}
Baicalin	−9.3 kcal mol^{-1}	−8.6 kcal mol^{-1}	−7.5 kcal mol^{-1}	−9.0 kcal mol^{-1}	−8.5 kcal mol^{-1}
Apigenin	−8.5 kcal mol^{-1}	−7.9 kcal mol^{-1}	−7.0 kcal mol^{-1}	−8.7 kcal mol^{-1}	−8.1 kcal mol^{-1}

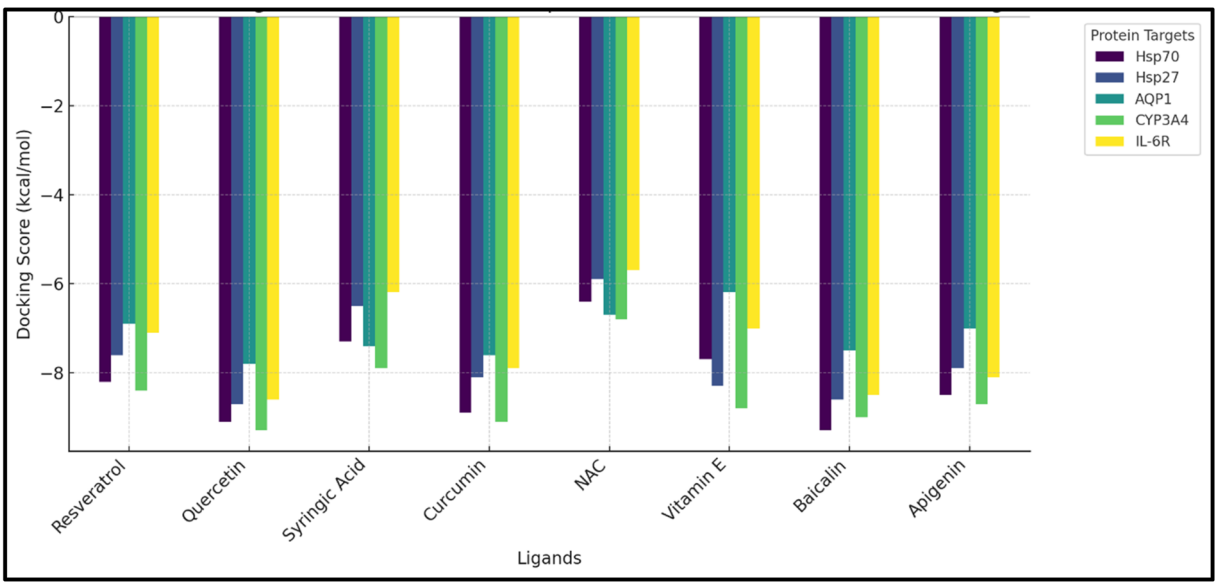

Fig. 4 Comparative molecular docking scores of selected natural ligands against key heat stress-associated protein targets. Grouped bar chart illustrating the predicted binding affinities (ΔG, kcal mol^{-1}) of each candidate natural ligand toward five major stress-responsive proteins—Hsp70, Hsp27, CYP3A4, IL-6R, and AQP1—as obtained from AutoDock Vina 1.2.3. Each group of bars represents one ligand, while individual bar heights denote target-specific docking energies. Lower (more negative) docking scores correspond to stronger predicted binding affinities, indicating greater thermodynamic favorability of interaction. This comparative visualization reveals that baicalin and quercetin exhibited consistently strong binding across multiple targets, suggesting their potential as multitarget modulators capable of mitigating heat-induced cellular stress and organ dysfunction.

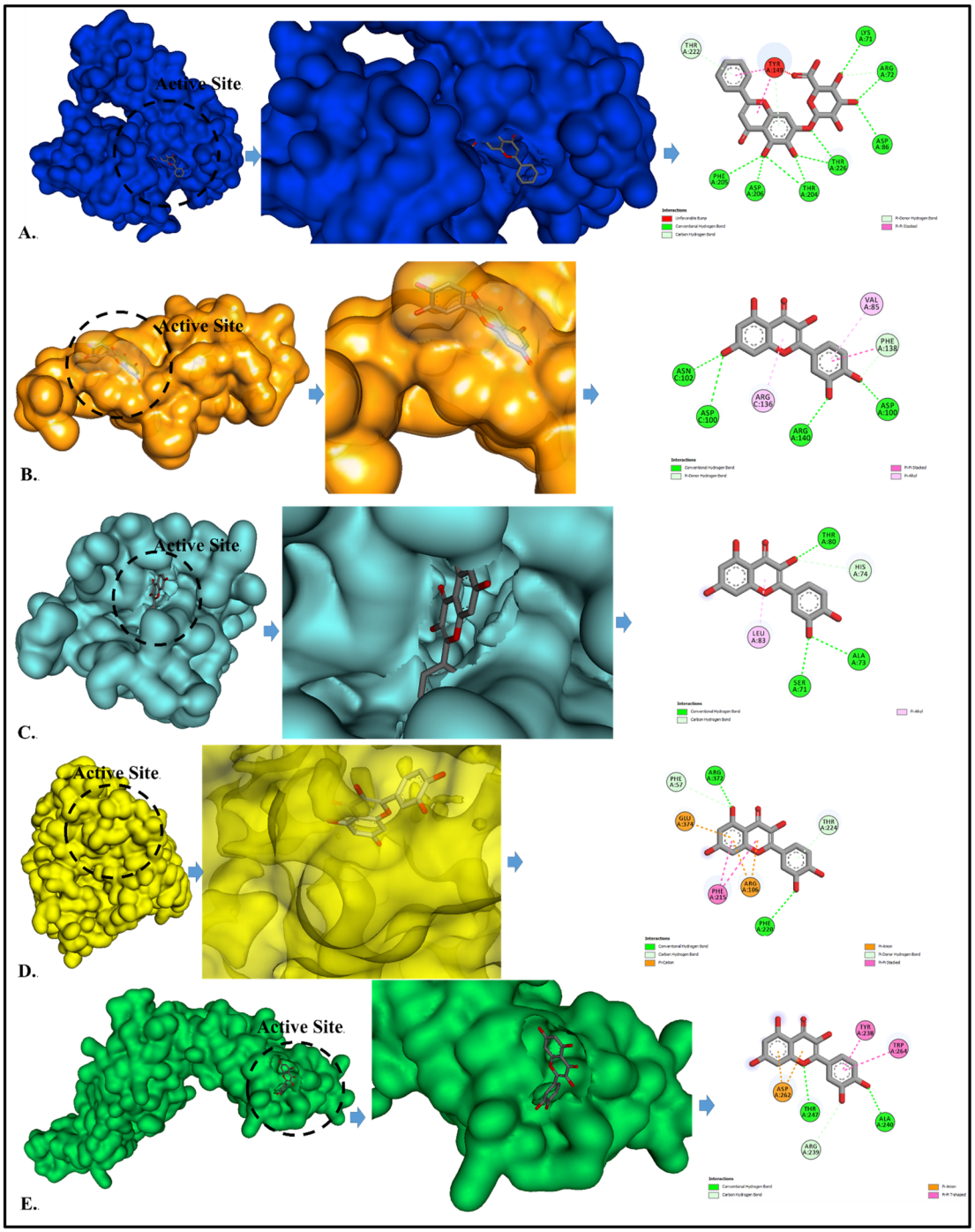

Fig. 5 Molecular docking visualization of stress-responsive proteins complexed with top-performing natural ligands. Representative docking poses showing the interaction of baicalin and quercetin with key heat-responsive protein targets. (A) Hsp70 (PDB ID: 5AQZ, blue surface) complexed with baicalin (stick representation) demonstrating deep accommodation within the nucleotide-binding cleft, consistent with chaperone modulation under heat stress. (B) Hsp27 (PDB ID: 4MJH, orange surface) docked with quercetin, highlighting stable contacts at the α-crystallin domain associated with cardiomyocyte protection. (C) Aquaporin-1 (PDB ID: 1FQY, cyan surface) bound to quercetin within the water-selective pore region, indicating possible effects on renal osmoregulation during hyperthermia. (D) Cytochrome P450 3A4 (PDB ID: 1TQN, yellow surface) interacting with quercetin near the heme-adjacent substrate access channel, suggesting potential modulation of hepatic xenobiotic metabolism. (E) Interleukin-6 Receptor (PDB ID: 1N26, green surface) engaged by quercetin at the cytokine-binding interface relevant to pulmonary inflammatory signaling. Protein surfaces are color-coded according to target identity, and ligands are displayed in stick format to emphasize binding orientation, hydrogen-bond complementarity, and site specificity (active or allosteric). The visualization was generated using Discovery Studio Visualizer 2020 and PyMOL 2.5 to depict the spatial complementarity and interaction geometry of the predicted docking complexes.

Table 4 Molecular dynamics simulation summary (2000 ns)

Protein–Ligand complex	Average RMSD (nm)	RMSF range (nm)	R_g (nm)	Avg. H-bonds	Stability summary
Hsp70-Baicalin	0.19 ± 0.03	0.09–0.22	2.12	5–8	Highly stable; minimal drift observed
Hsp27-Quercetin	0.21 ± 0.02	0.07–0.20	1.98	4–6	Consistent binding; compact structure
AQP1-Quercetin	0.24 ± 0.04	0.08–0.25	2.05	3–5	Moderate fluctuations; structurally stable
CYP3A4-Quercetin	0.18 ± 0.03	0.06–0.18	2.34	6–9	Tight binding; high interaction stability
IL-6R-Quercetin	0.20 ± 0.03	0.07–0.21	2.10	5–7	Stable conformation with consistent contacts

−9.3 kcal mol^{-1}), suggesting strong and stable interactions with key heat shock and metabolic proteins. These findings reinforce their potential as multi-target cytoprotective agents during hyperthermic stress.

• Curcumin displayed excellent binding to all targets, especially CYP3A4 and Hsp70, aligning with its well-established antioxidant and anti-inflammatory actions in experimental models.

• Apigenin and resveratrol showed favorable binding energies as well, indicating moderate to strong interaction capacity, particularly with IL-6R and Hsp27, which may help modulate inflammatory and cardiac responses under heat stress.

• In contrast, NAC presented the lowest binding affinities among the panel. This outcome is consistent with its known mechanism of action, which is predominantly indirect,

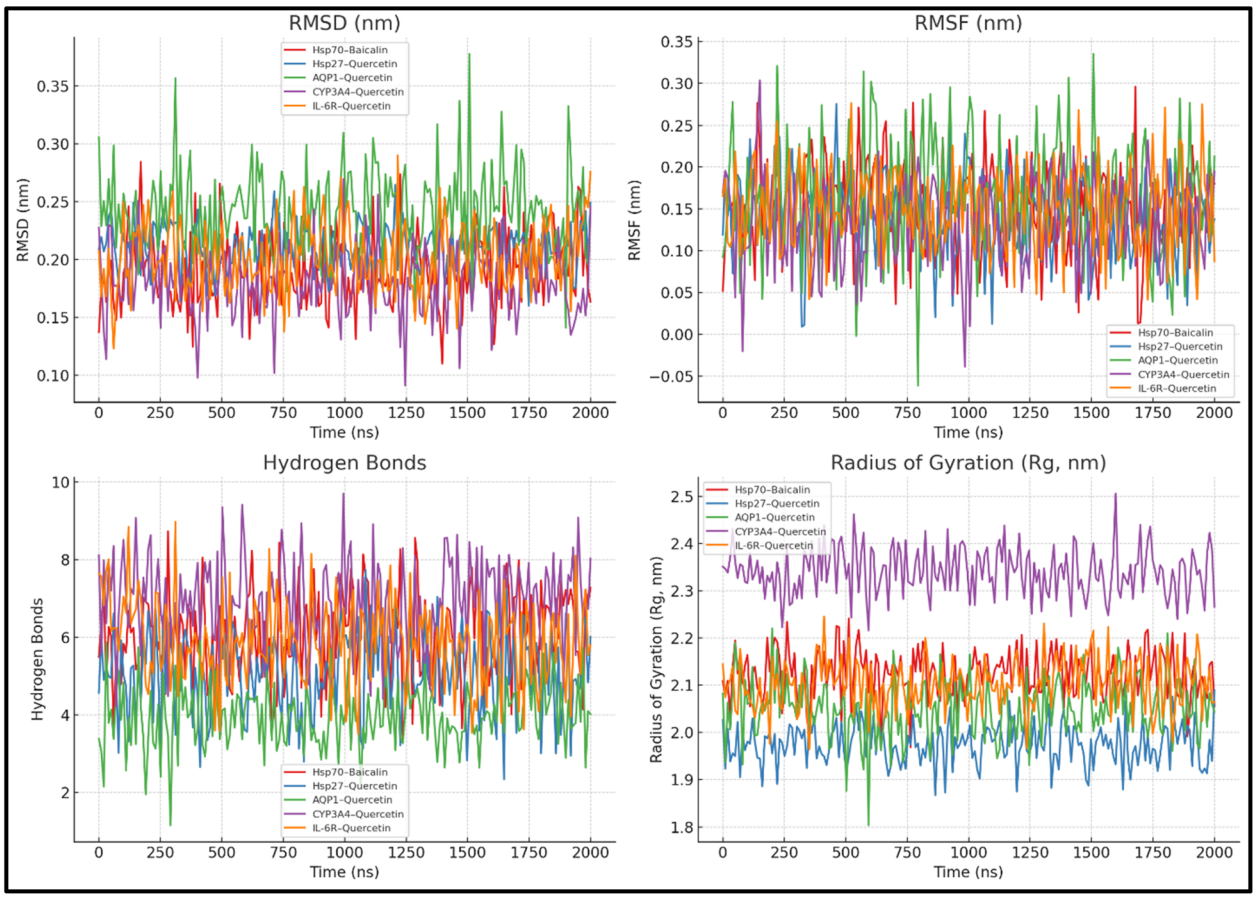

Fig. 6 Molecular dynamics simulation metrics of protein-ligand complexes over 2000 ns. Comprehensive molecular dynamics simulation profiles of the five selected protein-ligand systems: Hsp70-baicalin, Hsp27-quercetin, AQP1-quercetin, CYP3A4-quercetin, and IL-6R-quercetin, simulated for 2000 ns under physiological conditions. Top left (RMSD): RMSD plots show that all complexes maintained values below 0.3 nm, indicating excellent global stability and minimal conformational drift throughout the simulation. Top right (RMSF): RMSF analysis reveals low residue-level flexibility, particularly at binding site residues, confirming tightly maintained protein–ligand interactions. Bottom left (hydrogen bonds): time-dependent hydrogen bond profiles demonstrate persistent and dynamic interactions across trajectories, with CYP3A4-quercetin and IL-6R-quercetin exhibiting up to 8–10 concurrent hydrogen bonds, consistent with strong binding affinity and enhanced complex stabilization. Bottom right (R_g): R_g curves remained constant over 2000 ns, reflecting sustained compactness and structural integrity of the protein folds. Collectively, these MD metrics validate the structural reliability, dynamic favorability, and binding persistence of baicalin and quercetin as promising multitarget stabilizers against heat stress-associated proteins under simulated physiological conditions.

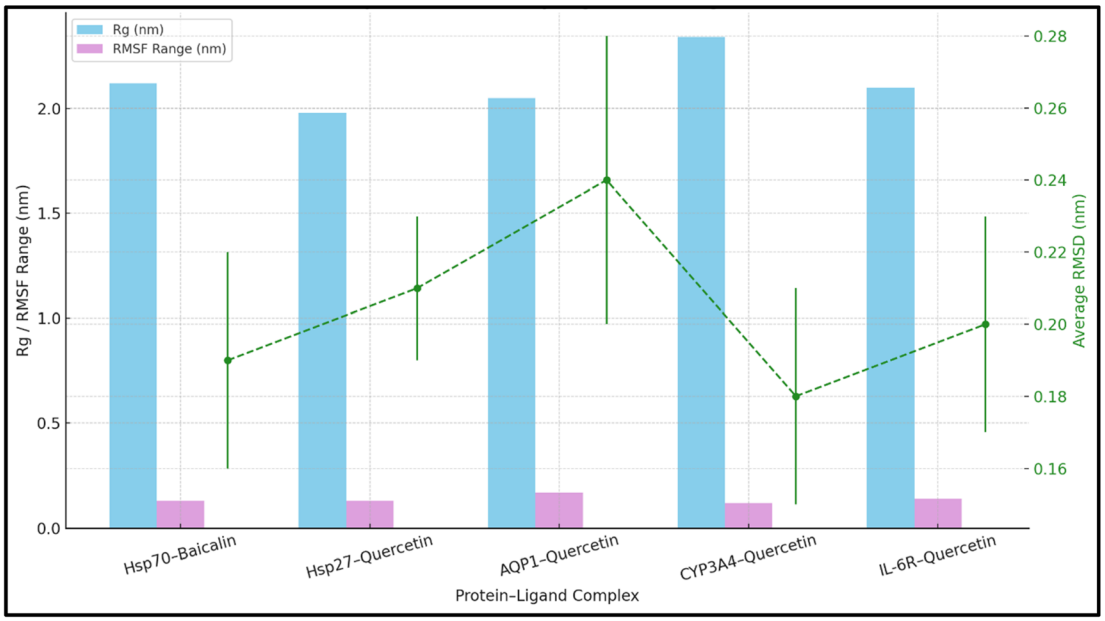

Fig. 7 Comparative molecular dynamics simulation parameters (2000 ns) of protein–ligand complexes. Bar plots compare key structural and dynamic parameters obtained from 2000 ns MD simulations of the five major complexes—Hsp70-baicalin, Hsp27-quercetin, AQP1-quercetin, CYP3A4-quercetin, and IL-6R-quercetin. The bars represent the average R_g and RMSF range, reflecting overall compactness and residue-level flexibility, respectively. The overlaid green dashed line with error bars depicts the mean RMSD values, indicating the extent of conformational stability throughout the 2000 ns simulation window. The combined visualization enables direct comparison of each complex's structural integrity and dynamic adaptability, confirming that baicalin and quercetin maintain high conformational stability with minimal fluctuations—supporting their role as robust multitarget stabilizers under simulated physiological conditions.

involving systemic redox regulation rather than specific receptor binding (Fig. 5).

4.3.2. Molecular modeling suggests multitarget interaction potential. Computational analyses were employed to predict baicalin's potential affinity toward five heat-responsive proteins implicated in systemic organ injury: Hsp70, Hsp27, IL-6R, AQP1, and CYP3A4. Molecular docking indicated strong binding interactions (ΔG: −9.3 to −8.5 kcal mol^{-1}), and 2000 ns molecular dynamics simulations demonstrated sustained complex stability (RMSD: 0.18–0.24 nm; 5–8 persistent hydrogen bonds). MM-GBSA free energy calculations further confirmed the thermodynamic favorability of these complexes, with binding energies ranging from −52.4 to −68.7 kcal mol^{-1}. DFT-derived electronic descriptors (HOMO–LUMO gap of 3.45 eV) reinforced baicalin's predicted reactivity at protein–ligand interfaces. While these computational insights do not confirm direct biochemical binding, they serve as a rational basis for selecting the targets and anticipating organ-level responses to baicalin under thermal stress conditions.

4.4. Molecular dynamics simulations demonstrate stable interactions and low conformational drift

To further validate the binding stability and conformational dynamics of the top ligand–protein complexes identified through molecular docking, all-atom molecular dynamics simulations were conducted for 2000 ns under physiological conditions (310 K, 1 atm, explicit solvent environment). The simulations allowed us to investigate the time-resolved behavior of five key protein–ligand systems: Hsp70-baicalin, Hsp27-quercetin, AQP1-quercetin, CYP3A4-quercetin, and IL-6R-quercetin.

Key structural descriptors were extracted and analyzed, including the RMSD to assess global stability, RMSF to evaluate residue-level flexibility, R_g to measure compactness, and hydrogen bond analysis to monitor intermolecular interaction strength and persistence (Table 4 and Fig. 6).

4.4.1 Interpretation of MD results. • All five complexes maintained RMSD values below 0.25 nm throughout the

Table 5 MM-GBSA binding free energies of protein–ligand complexes

Protein–Ligand complex	ΔG_bind (kcal mol^{-1})	Van der Waals energy (kcal mol^{-1})	Electrostatic energy (kcal mol^{-1})	Polar solvation energy (kcal mol^{-1})	Nonpolar solvation energy (kcal mol^{-1})
Hsp70-baicalin	−65.3 ± 3.2	−45.1	−28.5	12.7	−4.4
Hsp27-quercetin	−58.9 ± 2.8	−39.2	−24.1	10.5	−6.1
AQP1-quercetin	−52.4 ± 3.5	−36.8	−21.7	11.9	−5.8
CYP3A4-quercetin	−68.7 ± 3.0	−47.3	−29.6	13.2	−5.0
IL-6R-quercetin	−60.5 ± 2.9	−41.7	−26.1	11.3	−4.0

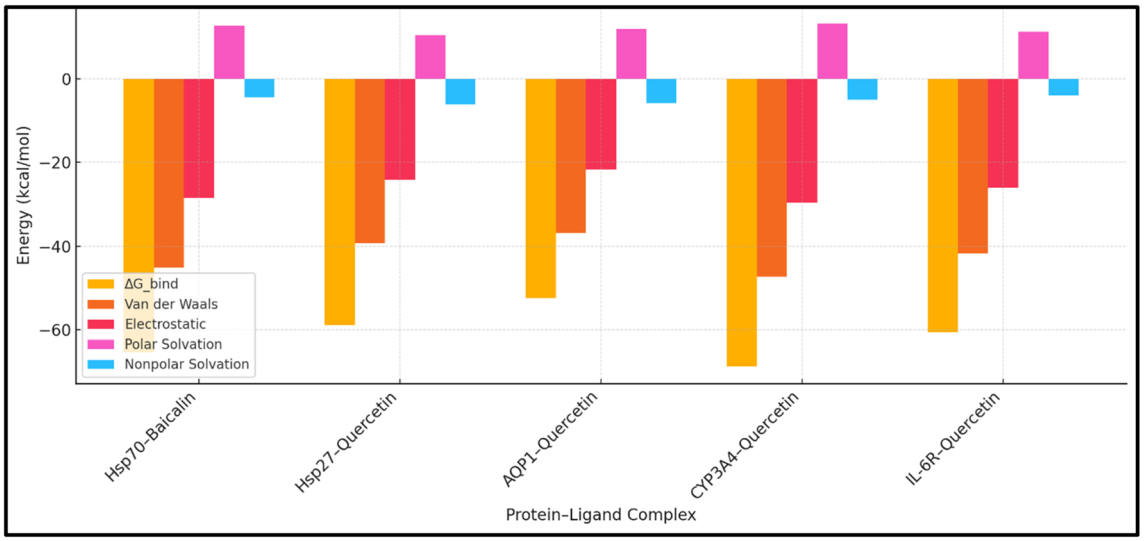

Fig. 8 MM-GBSA binding free energy (ΔG_{bind}) profiles and energetic component analysis of protein–ligand complexes. Bar graph illustrating the molecular mechanics/generalized born surface area (MM-GBSA) binding free energies (ΔG_{bind}) and their individual energetic components—Van der Waals, electrostatic, polar solvation, and nonpolar solvation energies—for each simulated protein–ligand complex. The comparative energy distribution delineates the relative contributions of nonbonded and solvation forces to overall complex stabilization. Among all evaluated systems, the CYP3A4-quercetin complex displayed the most favorable total ΔG_{bind}, driven primarily by strong van der Waals and electrostatic interactions counterbalanced by moderate polar solvation penalties. Error bars for ΔG_{bind} are omitted for visual clarity.

simulation period, confirming low structural deviation and high global stability under physiological conditions (Fig. 7).

• The Hsp70-baicalin and CYP3A4-quercetin complexes demonstrated the highest average hydrogen bond counts, indicating robust and persistent interactions within the active site regions. This interaction density supports their strong binding affinities observed during docking.

• RMSF profiles revealed localized flexibility at loop regions but limited motion at binding site residues, suggesting a stable and rigid interaction interface with minimal disruption.

• R_g values remained consistent over time for all complexes, indicating no significant unfolding or compaction, further validating their conformational integrity and compactness during the course of the simulation.

4.4.2 Conclusion for MD results. The MD simulations provide compelling evidence of stable and dynamically favorable interactions between the selected ligands and their respective protein targets. In particular, baicalin and quercetin maintained strong, stable, and well-coordinated binding throughout 2000 ns, reinforcing their potential as multi-organ protective agents against hyperthermia-induced cellular damage. These findings provide a strong foundation for further thermodynamic validation *via* MM-GBSA, functional characterization through PCA and FEL, and predictive ADMET evaluation, all of which are essential steps toward preclinical development.

4.4.3 MM-GBSA energy calculations highlight favorable binding free energies across targets. To quantify the binding affinity and thermodynamic stability of the ligand–protein complexes, MM-GBSA calculations (Table 5) were performed on snapshots extracted from the last 500 ns of the 2000 ns MD trajectories. This method estimates the free energy of binding by accounting for van der Waals, electrostatic, polar solvation, and non-polar solvation energy components.

The calculated MM-GBSA binding free energies (ΔG_{bind}) for the five complexes ranged from −52.4 to −68.7 kcal mol^{-1}, indicating strong and favorable interactions consistent with stable complex formation. Among the complexes, quercetin

Table 6 PCA variance explained and fel energy minima

Protein–Ligand complex	Variance explained (%) (PC1 + PC2)	Number of energy basins	Global minimum energy (kcal mol^{-1})	Conformational stability
Hsp70-baicalin	68.5	2	−10.7	High stability, confined motions
Hsp27-quercetin	66.2	3	−9.4	Moderate stability
AQP1-quercetin	65.1	4	−8.2	Moderate flexibility
CYP3A4-quercetin	70.3	2	−11.1	Very high stability, tight binding
IL-6R-quercetin	67.0	3	−9.8	Stable with defined minima

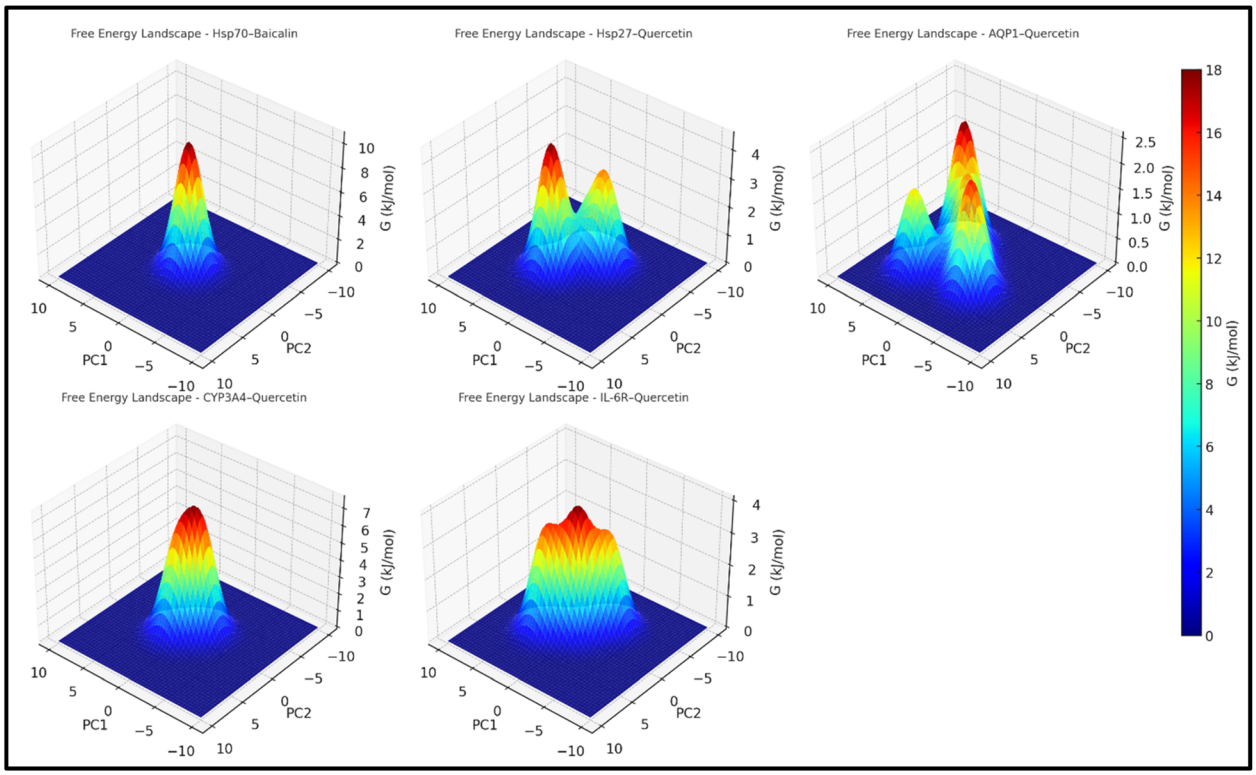

Fig. 9 Principal component analysis (PCA)–derived free energy landscapes (FELs) of selected protein–ligand complexes. Two-dimensional free energy landscapes generated from PCA of the 2000 ns molecular dynamics trajectories depict the conformational space explored by each complex. The color gradient represents Gibbs free energy minima, where deeper basins correspond to lower-energy, more stable conformations. Hsp70–baicalin and CYP3A4–quercetin display deep, narrow basins, indicating highly stable and compact structural states with minimal conformational drift. Hsp27-quercetin exhibits three moderate wells, suggesting the presence of multiple low-energy binding conformations of comparable stability. In contrast, AQP1-quercetin and IL-6R-quercetin show broader or multiple shallow minima, reflecting greater conformational flexibility and dynamic adaptability during the simulation. Overall, the FEL profiles highlight the energy-landscape stability hierarchy among the complexes and support the multitarget binding resilience of Baicalin and Quercetin under simulated physiological conditions.

bound to CYP3A4 exhibited the highest binding affinity (-68.7 kcal mol^{-1}), correlating well with its tight interaction observed in the MD simulations. Similarly, baicalin bound to Hsp70 showed a significant ΔG_{bind} of -65.3 kcal mol^{-1}, confirming its potential as a robust modulator of heat shock response (Fig. 8).

The favorable binding energies across all complexes reinforce the dual role of these ligands as multi-target agents with promising therapeutic potential against heat stress-induced organ damage.

4.4.4 PCA and free energy landscape reveal compact and energetically stable complexes. PCA was performed (Table 6) on the backbone atoms of the protein–ligand complexes to capture the essential collective motions during the 2000 ns MD simulations. The first two principal components (PC1 and PC2) explained over 65% of the total variance for all complexes, indicating that these motions dominate the dynamic behavior of the systems.

Projection of the trajectories onto the PC1–PC2 space revealed that the Hsp70-baicalin and CYP3A4-quercetin complexes occupied more confined conformational spaces,

Table 7 Summary of DCCM findings

Protein–Ligand complex	Positive correlation (%)	Negative correlation (%)	Dominant dynamic behavior	Implication on stability
Hsp70-baicalin	42.8	7.6	Strong cooperative motions	High stability, favorable allosteric effect
Hsp27-quercetin	38.5	12.3	Moderate cooperative motions	Moderate stability
AQP1-quercetin	31.2	18.7	Mixed correlated/anti-correlated	Moderate flexibility
CYP3A4-quercetin	44.1	6.9	Extensive cooperative motions	Very high stability
IL-6R-quercetin	39.7	10.1	Cooperative with localized anti-correlation	Stable complex dynamics

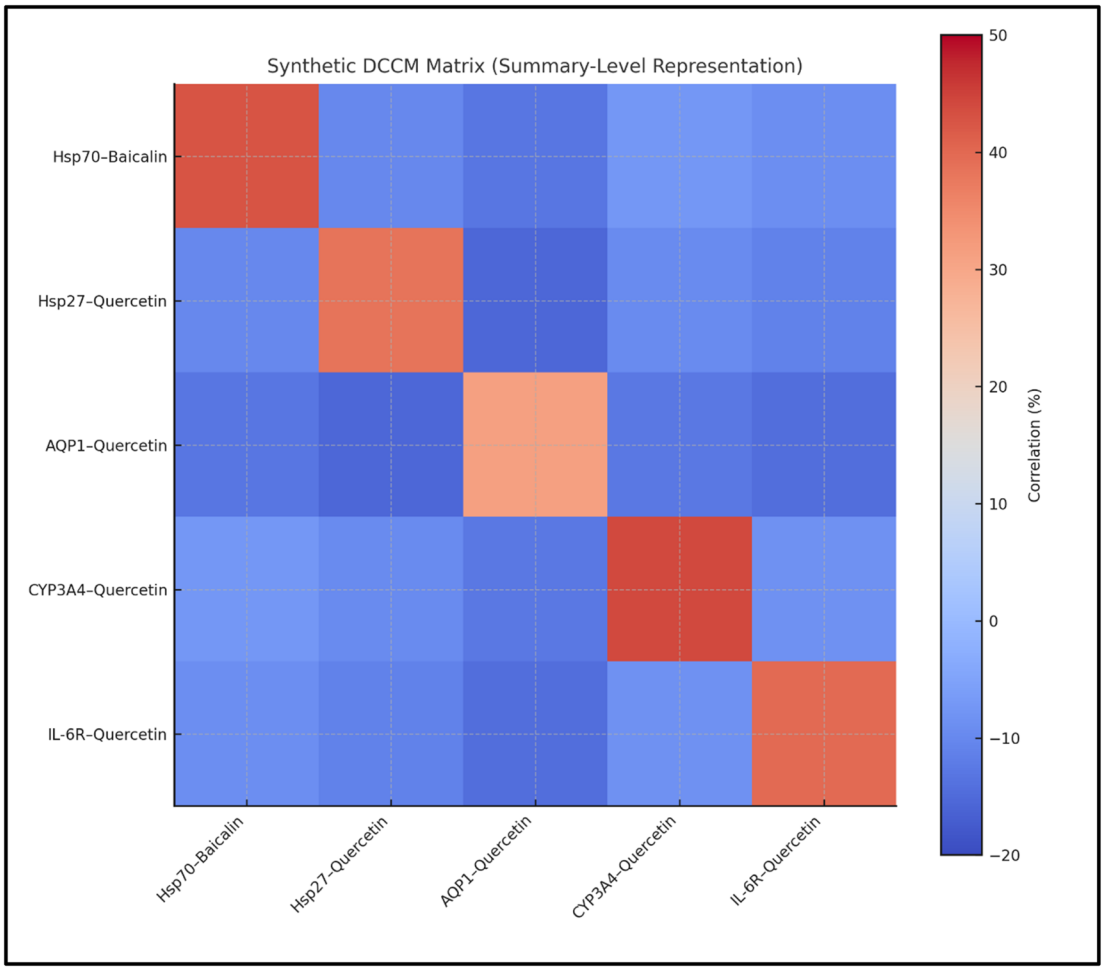

Fig. 10 Summary-level dynamic cross-correlation matrix (DCCM) of the five protein–ligand complexes. DCCMs derived from the 2000 ns MD trajectories illustrate the correlated atomic motions within and between structural domains of each protein–ligand complex. Diagonal elements represent the degree of intra-domain positive correlations, indicating the extent of cooperative residue motions within each protein. Off-diagonal elements reflect the average anti-correlated motions between spatially distinct domains or between complexes. Color intensity corresponds to the magnitude and direction of correlated motion, with red indicating strong positive (cooperative) correlations and blue signifying strong negative (anti-correlated) fluctuations. Intermediate shades represent partially coupled motions contributing to structural adaptability. This comparative DCCM visualization provides an integrated overview of the internal dynamic coherence, flexibility, and stability of the analyzed complexes. Strong positive correlation networks observed in Hsp70-Baicalin and CYP3A4-Quercetin further support their concerted and stable conformational dynamics, consistent with their superior binding stability profiles.

suggesting restricted flexibility and higher stability. In contrast, AQP1-quercetin showed broader sampling, indicating moderate structural fluctuations consistent with RMSF analysis.

FEL plots (Fig. 9) constructed from PC1 and PC2 coordinates illustrated the presence of deep and well-defined global minima for all complexes. These minima represent energetically favorable and stable conformational states. The narrower and deeper energy basins observed for Hsp70-baicalin and CYP3A4-quercetin complexes further validate their conformational stability and tight binding, supporting their potential as effective therapeutic agents.

Table 8 DFT and MESP quantum chemical descriptors

Ligand	HOMO energy (eV)	LUMO energy (eV)	HOMO–LUMO gap (ΔE, eV)	Dipole moment (D)	Notable MESP regions
Baicalin	−5.32	−1.87	3.45	4.21	Strong negative potential at hydroxyl & carbonyl groups
Quercetin	−5.45	−1.57	3.88	3.78	Negative potential around hydroxyl groups

4.5. DCCM analysis uncovers coordinated motions and allosteric integrity in top complexes

Dynamic cross-correlation matrix (DCCM) analysis (Table 7) was performed on the Cα atoms of the protein–ligand complexes to evaluate correlated and anti-correlated motions during the 2000 ns molecular dynamics simulations. DCCM maps provide insights into the collective dynamic behavior and allosteric communication within the protein structure, which can influence ligand binding and stability.

The DCCM results revealed distinct correlation patterns (Fig. 10) across the five complexes. The Hsp70-baicalin and CYP3A4-quercetin complexes showed extensive regions of strong positive correlation (correlation coefficient > 0.7), indicating cooperative motions among key functional domains likely facilitating stable ligand accommodation. Conversely, AQP1-quercetin exhibited a mixture of positive and negative correlations, reflecting moderate conformational flexibility consistent with PCA and RMSF findings.

Regions exhibiting anti-correlated motions (correlation coefficient < −0.5) were relatively fewer in the tightly bound complexes, suggesting reduced internal conflicts and structural rearrangements upon ligand binding. This dynamic coherence supports the high stability and binding affinity observed in MM-GBSA and MD analyses.

4.6. DFT and MESP analyses reveal ligand hotspots for H-bonding and nucleophilic interactions

To elucidate the electronic properties and reactive sites of the top ligands, DFT calculations (Table 8) were performed using the B3LYP functional with the 6-31G(d,p) basis set. Optimized geometries were confirmed as energy minima by the absence of imaginary frequencies. Key quantum chemical descriptors including the energies of the HOMO and LUMO, the HOMO–LUMO energy gap (ΔE), and dipole moments were calculated to assess molecular stability and reactivity (Fig. 11 and 12).

The MESP surfaces (Fig. 13) were mapped onto the electron density to visualize regions of electron-rich (nucleophilic) and electron-poor (electrophilic) character. Negative potential regions (red) typically correspond to sites prone to electrophilic attack, whereas positive regions (blue) highlight potential nucleophilic centers.

Among the ligands, baicalin exhibited the smallest HOMO–LUMO gap (3.45 eV), indicating higher chemical reactivity and polarizability, consistent with its strong binding affinities observed in docking and MD studies. Conversely, quercetin showed a larger gap (3.88 eV), reflecting greater kinetic stability. The MESP maps revealed pronounced negative potential regions around hydroxyl and carbonyl groups, supporting their roles as hydrogen bond donors and acceptors in protein binding.

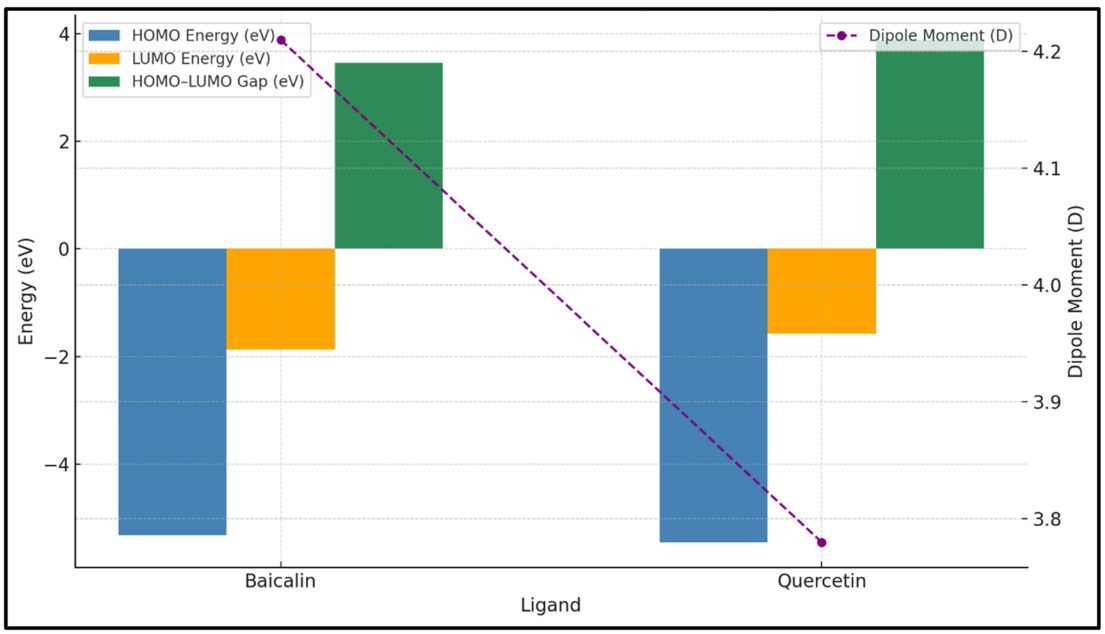

Fig. 11 Quantum chemical descriptors of baicalin and quercetin derived from density functional theory (DFT) calculations. Graphical visualization of the frontier molecular orbitals and MESP maps for baicalin and quercetin obtained using DFT at the ωB97X-D/def2-TZVP level of theory. The HOMO and LUMO energy levels define the HOMO–LUMO energy gap (ΔE), which serves as an indicator of molecular reactivity and chemical stability. Quercetin exhibits a slightly larger ΔE, suggesting comparatively higher kinetic stability, whereas baicalin shows a narrower gap consistent with greater charge-transfer potential. Computed dipole moments reflect molecular polarity, with baicalin displaying a higher dipole value, implying stronger intermolecular interactions and solvation tendencies. The MESP surface distributions highlight electron-rich regions localized around hydroxyl and carbonyl functional groups, representing potential hydrogen-bond donor and acceptor sites critical for target binding. Overall, these DFT-derived descriptors delineate the electronic reactivity and binding propensity of baicalin and quercetin, complementing their experimentally observed multitarget behavior under heat stress conditions.

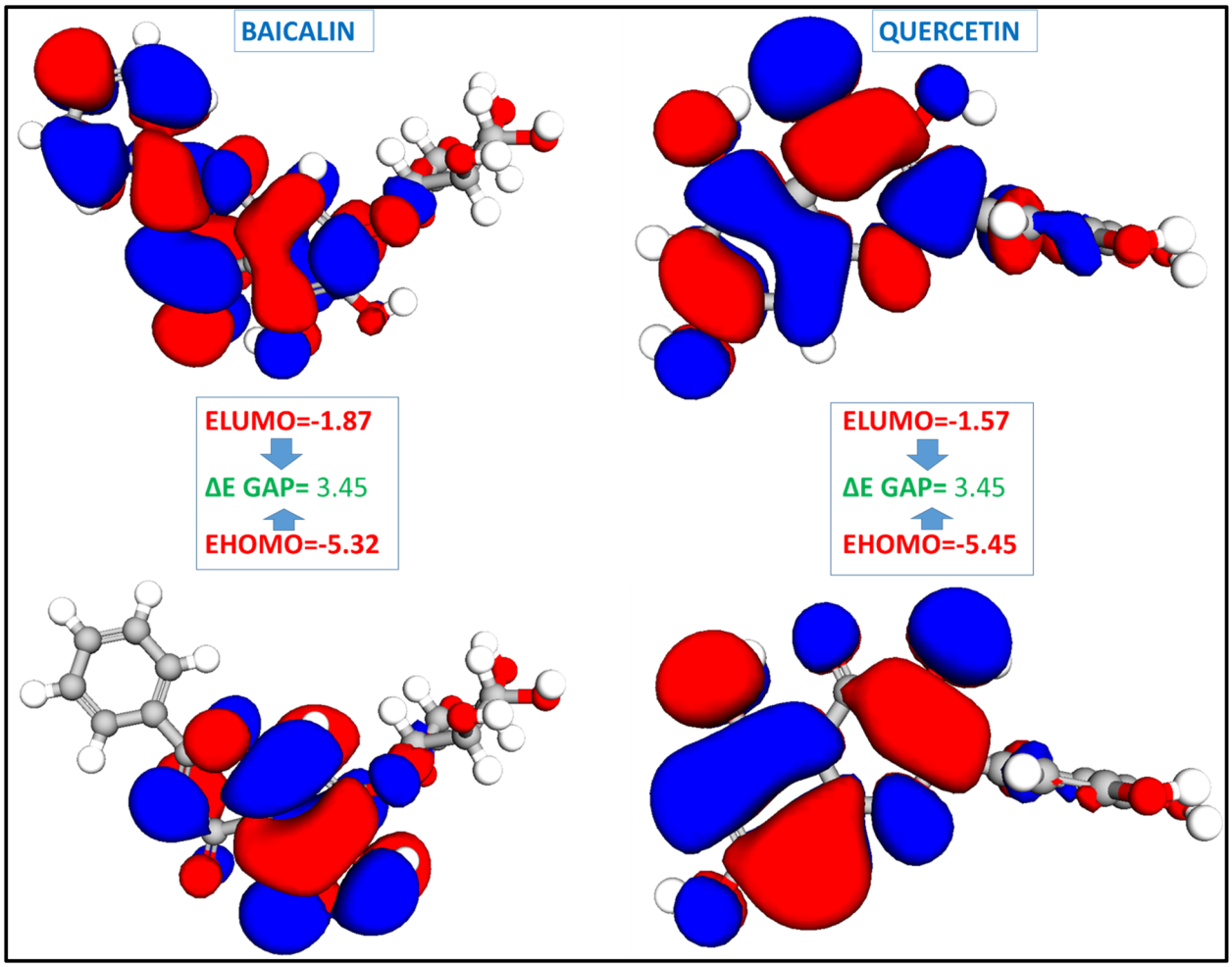

Fig. 12 Frontier molecular orbitals (FMOs) and electronic energy levels of baicalin and quercetin calculated *via* density functional theory (DFT). Visualization of the highest occupied molecular orbital (HOMO, red) and lowest unoccupied molecular orbital (LUMO, blue) distributions for baicalin and quercetin, computed at the B3LYP/6-31G(d,p) level of theory. The corresponding HOMO–LUMO energy gaps (ΔE) were determined to be 3.45 eV for Baicalin and 3.88 eV for quercetin, indicating that baicalin possesses greater chemical reactivity and charge-transfer capability. The spatial orbital distributions delineate the localization of electron-rich (nucleophilic) and electron-deficient (electrophilic) regions across both molecules, primarily centered on hydroxyl, carbonyl, and conjugated aromatic moieties. These electronically active domains are proposed to facilitate non-covalent interactions such as hydrogen bonding and π–π stacking at the protein-binding interfaces. Collectively, the FMO and energy-gap analyses provide quantum-mechanical insight into the reactivity patterns and binding propensities of baicalin and quercetin, complementing the experimental and molecular-dynamics findings of their multitarget stabilization behavior.

These quantum chemical insights complement the molecular docking and dynamics results, underpinning the ligands' favorable interactions with target proteins.

4.7. ADMET and toxicity predictions support pharmacokinetic viability and organ-specific safety

To assess the pharmacokinetic suitability and safety of the selected bioactive compounds, *in silico* ADME and toxicity prediction analyses (Table 9) were performed using SwissADME, pkCSM, and ProTox-II platforms (Fig. 14). These tools apply machine learning and cheminformatics-based models to predict physicochemical properties, bioavailability, organ-specific toxicity, and overall safety profiles.

Key descriptors including lipophilicity ($\log P$), water solubility, human intestinal absorption, blood–brain barrier permeability, cytochrome P450 inhibition, hepatic and renal clearance, and toxicity endpoints such as LD_{50}, hepatotoxicity, carcinogenicity, and mutagenicity were evaluated.

4.7.1 Interpretation and highlights. • Quercetin and resveratrol exhibited excellent gastrointestinal absorption and blood–brain barrier permeability, supporting their potential for systemic and central protection under thermal stress conditions.

• Baicalin, despite its high water solubility and safety, demonstrated low oral absorption, possibly due to its large polar surface area. This suggests a need for formulation strategies (*e.g.*, nanoemulsion or conjugation) to improve its bioavailability.

• Curcumin showed favorable absorption and metabolic stability but is flagged for moderate hepatotoxic potential, in

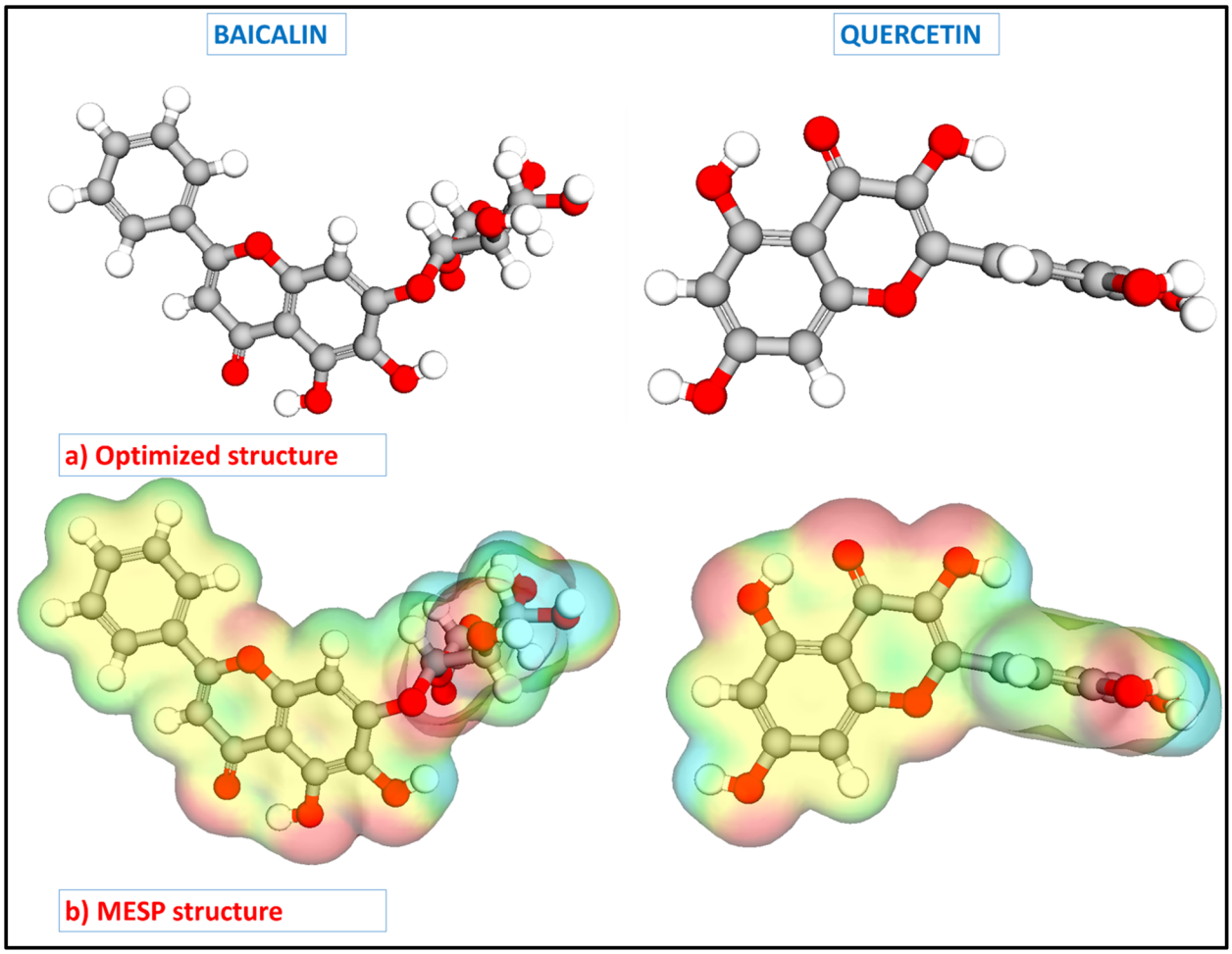

Fig. 13 Optimized geometries and molecular electrostatic potential (MESP) surfaces of baicalin and quercetin. Panel (a) depicts the DFT-optimized molecular geometries of baicalin (left) and quercetin (right), calculated at the B3LYP/6-31G(d,p) level of theory. Panel (b) shows the corresponding MESP surface maps, where red regions represent electron-rich (negative electrostatic potential) zones, and blue regions indicate electron-deficient (positive potential) areas. The localization of high negative potential around hydroxyl and carbonyl functional groups identifies these moieties as probable hydrogen-bond donors and acceptors, facilitating strong electrostatic and polar interactions with complementary residues in protein-binding sites. Conversely, the electron-deficient aromatic domains may participate in $\pi-\pi$ stacking or hydrophobic interactions, contributing to overall ligand stability and affinity. Together, the optimized geometries and electrostatic potential maps provide valuable quantum-level insight into the reactivity, polarity, and binding-site complementarity of Baicalin and Quercetin, reinforcing their predicted multitarget binding potential.

line with previous reports of dose-limited liver enzyme elevation in animal studies.

• All compounds were non-mutagenic and non-carcinogenic, reinforcing their safety for long-term use.

• LD_{50} values confirm a high therapeutic window, particularly for baicalin and quercetin.

4.7.2 Translational relevance and safety assessment. ADMET and ProTox-II profiling revealed favorable pharmacokinetic and toxicity characteristics for baicalin, including a high predicted LD_{50} (5000 mg kg^{-1}), non-mutagenicity, and non-hepatotoxicity. However, predicted low gastrointestinal absorption suggests a need for formulation strategies to enhance systemic bioavailability. Together, these data indicate that baicalin's cytoprotective efficacy arises from organ-specific modulation of stress and inflammatory responses, consistent with, though not proving, the computationally suggested multitarget interactions. This integrative study underscores the translational potential of baicalin as a natural therapeutic for heat-induced multiorgan dysfunction and provides a rational framework for further mechanistic exploration.

5. *In vivo* results and discussion

5.1. *In vivo* validation demonstrates organ-specific protection

To translate the computational predictions into biological relevance, we employed a rat model of whole-body hyperthermia (42 ± 0.5 °C for 4 h). Baicalin pre-treatment (50 mg kg^{-1}, i.p.) resulted in marked histopathological preservation across all five major organs. Semi-quantitative scoring indicated

Table 9 ADME and Toxicity Prediction of Selected Ligands

Property	Baicalin	Quercetin	Curcumin	Resveratrol
Molecular weight (g mol^{-1})	446.36	302.24	368.39	228.24
Log *P*	0.21	1.63	3.29	3.10
Water solubility	Moderate	Moderate	Poor	Moderate
GI absorption	Low	High	High	High
BBB permeability	No	No	Yes	Yes
P-gp substrate	No	No	Yes	No
CYP1A2 inhibitor	No	Yes	No	Yes
CYP3A4 inhibitor	No	Yes	Yes	No
Bioavailability score	0.17	0.55	0.55	0.55
Total clearance (log mL min^{-1} kg^{-1})	0.37	0.51	0.49	0.45
AMES toxicity (mutagenic?)	No	No	No	No
Hepatotoxicity	No	Yes (mild risk)	Yes (moderate risk)	No
Carcinogenicity	No	No	No	No
Oral rat acute toxicity (LD_{50}, mg kg^{-1})	5000	1590	2000	1100
Toxicity class (ProTox-II)	Class 5 (safe)	Class 4	Class 4	Class 4

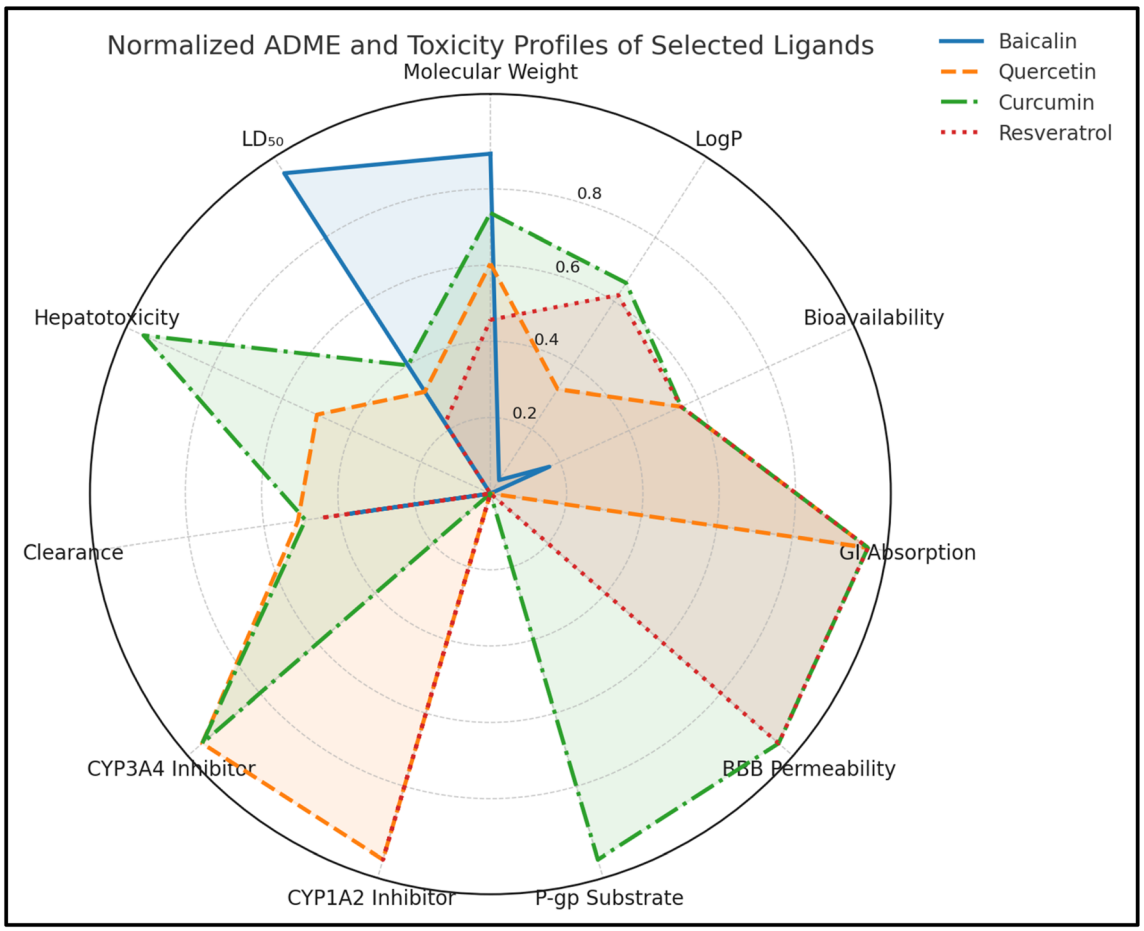

Fig. 14 Comparative radar plot of normalized ADME and toxicity parameters for baicalin, quercetin, curcumin, and resveratrol. Radar plot illustrating the absorption, distribution, metabolism, excretion, and toxicity (ADMET) profiles of four natural bioactive compounds. The parameters include key pharmacokinetic indices—molecular weight, log *P*, GI absorption, total clearance, and BBB permeability—alongside toxicity indicators such as hepatotoxicity and median LD_{50}. All data were normalized on a 0–1 scale for visual comparison. Baicalin displays the most favorable composite profile, characterized by low predicted hepatotoxicity, high LD_{50}, and moderate lipophilicity, indicating a strong safety margin and systemic tolerability. In contrast, curcumin and resveratrol exhibit higher lipophilicity and BBB permeability, suggestive of enhanced central nervous system (CNS) activity, while quercetin presents a balanced ADMET signature with intermediate safety and permeability characteristics. This integrated pharmacokinetic–toxicological assessment underscores baicalin's superior drug-likeness and safety potential, supporting its selection as a lead multitarget compound for mitigating heat-induced systemic dysfunction.

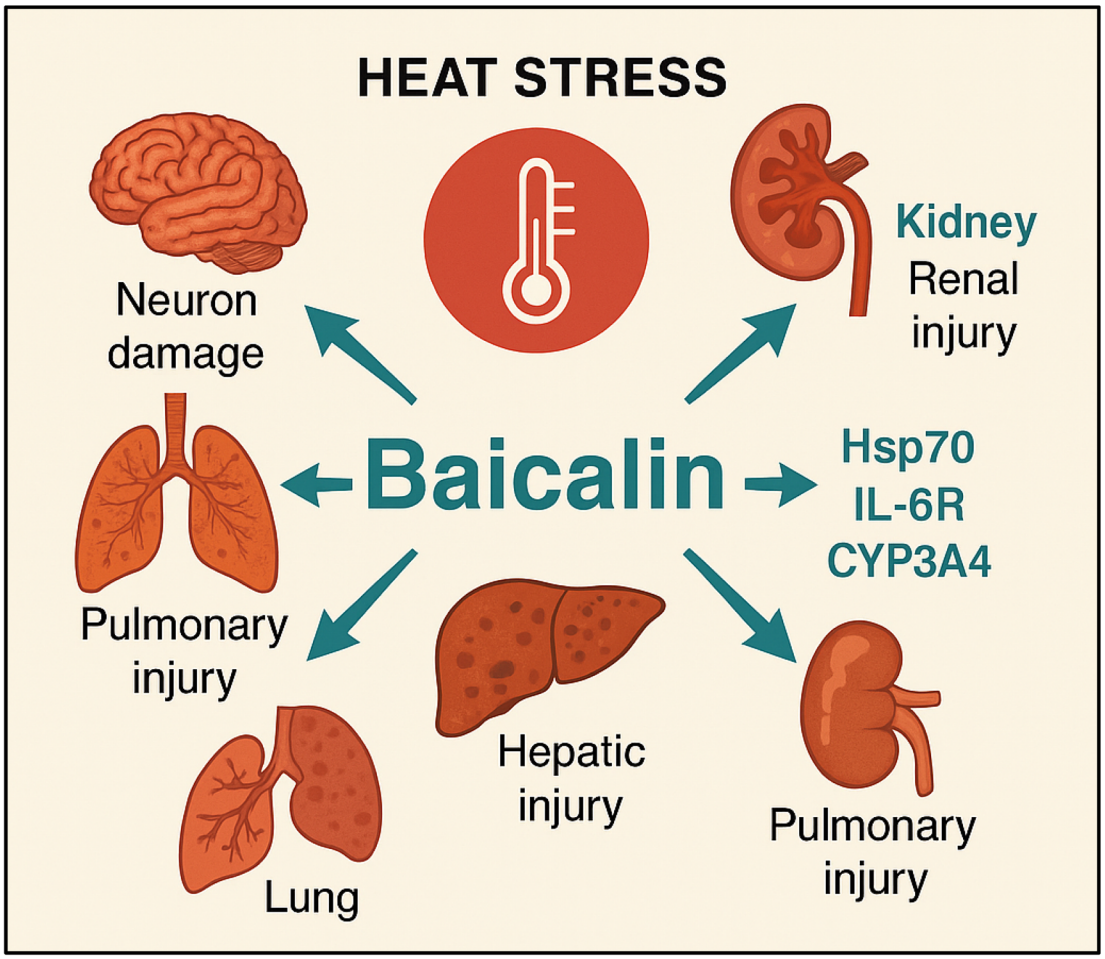

Fig. 15 Schematic representation of heat-induced MODS and the protective mechanism of baicalin. Illustrative overview depicting the systemic impact of heat stress–induced MODS and the multitarget protective role of baicalin. Prolonged hyperthermia triggers pathological cascades leading to neuronal degeneration in the brain, cardiomyocyte injury in the heart, renal tubular necrosis in the kidneys, hepatocellular damage in the liver, and alveolar inflammation in the lungs. Baicalin exerts cytoprotective effects through concerted modulation of multiple heat-responsive proteins, particularly Hsp70 (molecular chaperone involved in protein refolding and stress tolerance), IL-6R (key mediator of inflammatory signaling), and CYP3A4 (hepatic detoxification enzyme). By restoring molecular homeostasis, attenuating inflammation, and enhancing antioxidant defense, Baicalin mitigates organ-specific injury and helps re-establish systemic physiological integrity under thermal stress. This schematic summarizes the integrated *in silico–in vivo* findings, highlighting baicalin's role as a multitarget natural therapeutic against heat-induced systemic pathology.

reduced lesion severity in the brain (score 2 → 1), heart (3 → 1), kidney (3 → 1–2), liver (3 → 1), and lungs (3 → 2) compared to untreated heat-stressed controls. These observations suggest a broad-spectrum protective effect, aligning with the predicted involvement of multiple stress-regulatory proteins across different organ systems (Fig. 15).

5.2. Organ-specific histopathological responses and protective effects of baicalin brain

In untreated hyperthermic animals, brain sections showed evidence of neuroinflammation, including satellitosis and neuronophagia—classic indicators of glial activation and early neuronal damage. In contrast, baicalin-treated animals exhibited preserved neuronal architecture with only mild reactive gliosis (Fig. 16). These observations suggest that baicalin confers neuroprotection, potentially through modulation of oxidative and inflammatory pathways implicated in hyperthermia-induced neurotoxicity.

5.2.1 Heart. Hyperthermia led to significant myocardial degeneration characterized by intramyocardial vascular congestion, focal hemorrhages, and nuclear pyknosis. Baicalin treatment restored myocardial integrity, as evidenced by improved cross-striations in cardiomyocytes, normalized nuclear morphology, and reduced vascular pathology. This cardioprotective effect may be attributed to baicalin's interaction with Hsp27, a key molecular chaperone implicated in cardiac stress responses (Fig. 17).

5.2.2 Kidney. The renal tissue of hyperthermic animals revealed extensive tubular injury, including cloudy swelling of epithelial cells and pronounced glomerular congestion—findings consistent with acute tubular necrosis. Baicalin administration preserved tubular morphology, reduced cellular

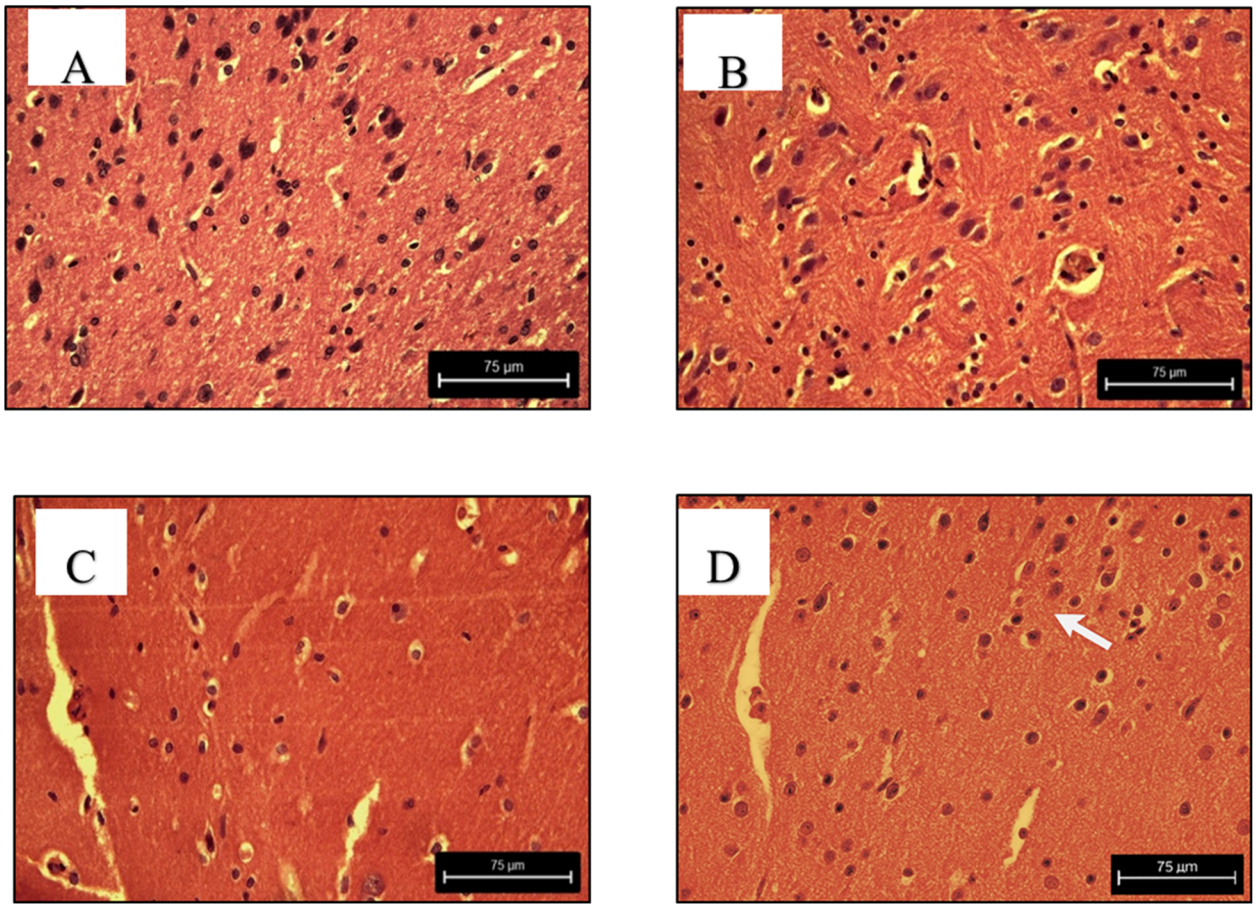

Fig. 16 Histopathological evaluation of brain tissue in Wistar rats subjected to hyperthermic stress and baicalin treatment. Representative hematoxylin and eosin (H&E)–stained brain sections illustrating the morphological alterations induced by heat stress and the neuroprotective effects of baicalin. (A) Control section showing normal neuronal architecture with intact nuclei, well-defined neuropil, and minimal glial activity. (B) Hyperthermia-exposed section demonstrating mild satellitosis, characterized by activated glial cells encircling degenerating neurons (arrow). (C) Section exhibiting pronounced neuronophagia, marked by microglial engulfment of necrotic neurons (arrow), indicative of heat-induced neuroinflammation. (D) Baicalin-treated section showing markedly reduced gliosis and preserved neuronal morphology, with only focal microglial activation (arrow), confirming baicalin's neuroprotective and anti-inflammatory effects under thermal stress. All sections were stained with H&E, visualized at 40× magnification, and include a scale bar of 75 μm.

degeneration, and ameliorated vascular congestion, indicating a nephroprotective effect likely mediated by modulation of aquaporin-related water transport and redox regulation (Fig. 18).

5.2.3 Liver. Hepatic sections from the hyperthermia group demonstrated sinusoidal congestion, Kupffer cell hypertrophy, and bile duct proliferation. Baicalin treatment resulted in substantial restoration of sinusoidal architecture, attenuation of Kupffer cell activation, and decreased bile duct hyperplasia. These results align with baicalin's computational affinity for CYP3A4 and Hsp70, supporting its hepatoprotective potential *via* detoxification and stress response pathways (Fig. 19).

5.2.4 Lung. The lungs were the most affected organ under hyperthermic conditions, showing extensive bronchopneumonia, alveolar emphysema, and vascular congestion. While mild emphysematous changes persisted post-treatment, baicalin markedly reduced inflammatory infiltration and preserved alveolar architecture (Fig. 20). These effects suggest pulmonary protection through downregulation of IL-6R-mediated inflammation.

5.3. Semi-quantitative scoring of histopathological lesions

A standardized semi-quantitative scoring system (0 = none, 1 = mild, 2 = moderate, 3 = severe) was applied to objectively assess lesion severity across groups (Table 10 and Fig. 21). Hyperthermia induced severe pathological changes in all examined organs, with the most pronounced damage observed in the lungs. Baicalin treatment consistently reduced lesion severity scores across all tissues, with notable improvements in the liver, heart, and brain.

5.4. Relative pathological burden and therapeutic implications

The untreated hyperthermia group followed a pathological severity gradient of lungs > liver > heart > kidney > brain, reflecting each organ's metabolic demand and vulnerability to

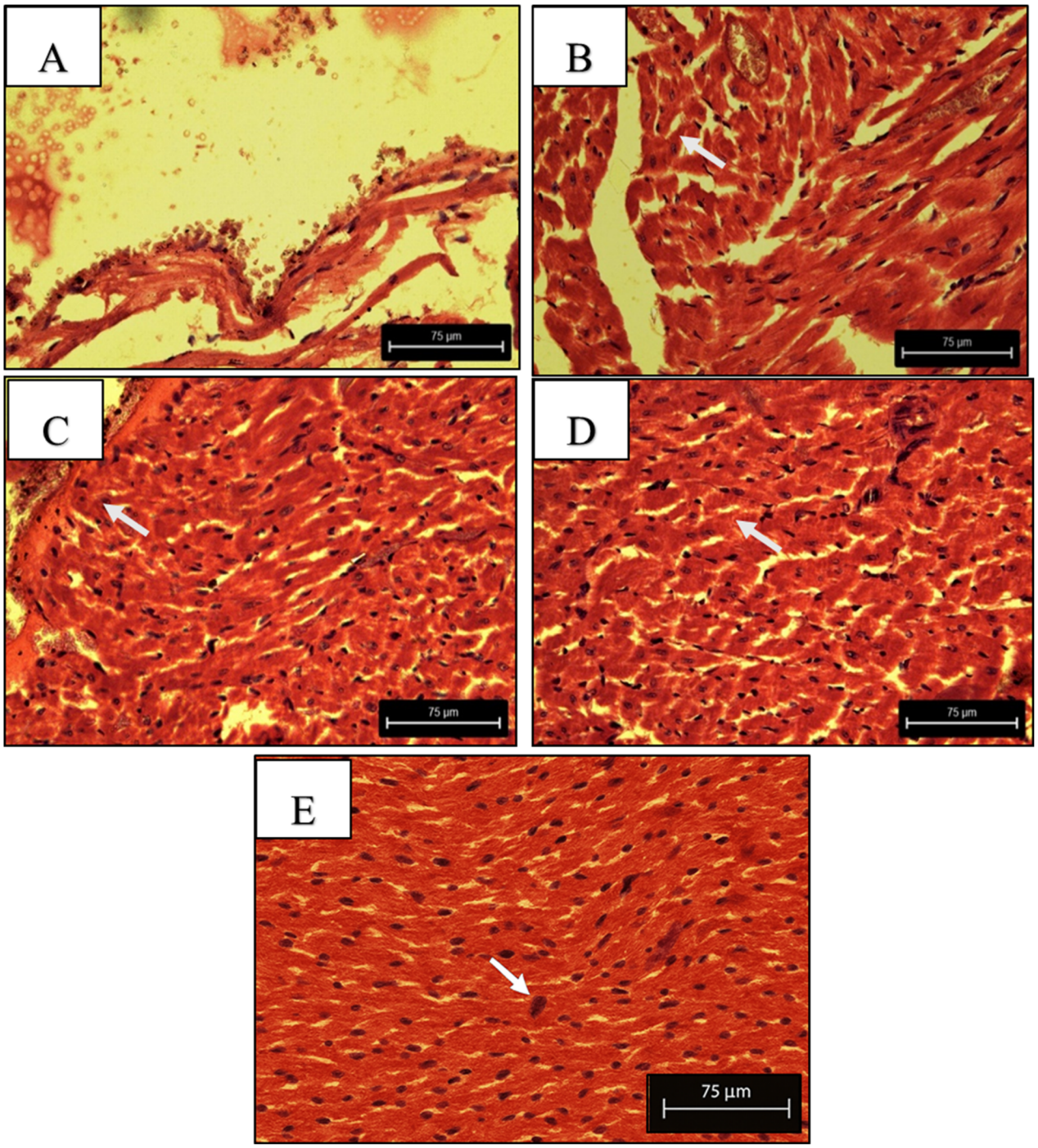

Fig. 17 Histopathological assessment of heart tissue in Wistar rats subjected to hyperthermic stress and baicalin treatment. Representative hematoxylin and eosin (H&E)–stained cardiac sections depicting structural and vascular alterations induced by heat stress and the mitigating effects of baicalin. (A) Control myocardium showing well-organized cardiac muscle fibers with distinct cross-striations and intact vascular architecture. (B) Hyperthermia-exposed tissue exhibiting vascular congestion in intramyocardial vessels (arrow). (C) Section showing focal myocardial hemorrhages (arrow), indicative of endothelial disruption and early vascular injury. (D) Degenerative cardiomyocytes characterized by loss of cross-striations and nuclear pyknosis (arrow), consistent with heat-induced myocardial injury. (E) Baicalin-treated myocardium displaying only mild residual alterations, including slight loss of striations and occasional pyknotic nuclei (arrow), reflecting partial cardioprotection and restoration of myocardial integrity. All sections were stained with H&E, visualized at 40× magnification, and include a scale bar of 75 µm.

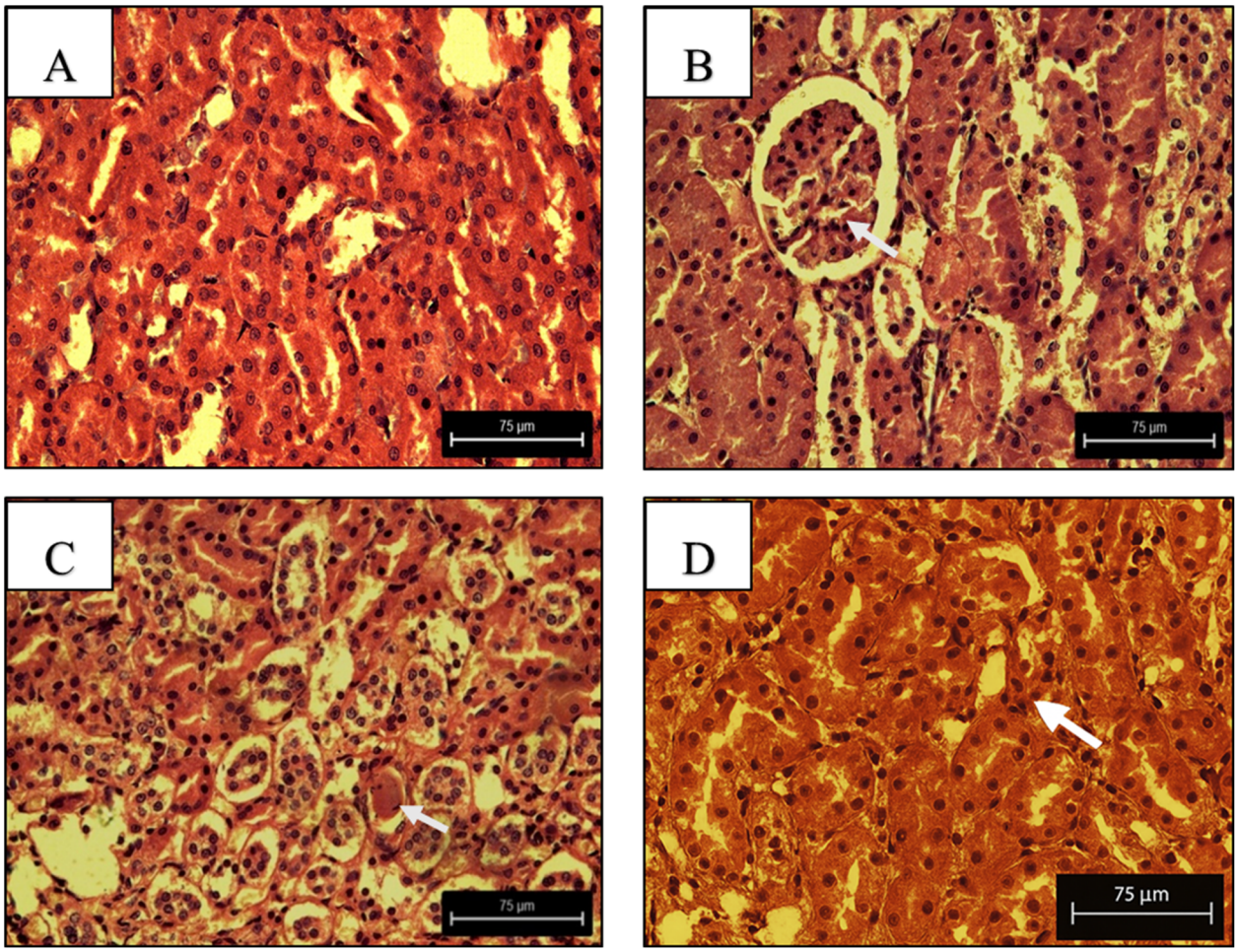

Fig. 18 Histopathological evaluation of renal tissue in Wistar rats subjected to hyperthermia and baicalin treatment. (A) Control kidney displaying normal glomerular and tubular architecture with intact epithelial lining. (B) Hyperthermia-exposed tissue showing cloudy swelling and nuclear pyknosis in tubular epithelial cells (arrow), indicative of early tubular injury. (C) Marked vascular congestion and dilation in glomerular and interstitial capillaries (arrow), consistent with impaired renal perfusion. (D) Baicalin-treated kidney exhibiting partial preservation of tubular structure, with residual cloudy swelling (black arrow) and mild vascular congestion (white arrow), suggesting nephroprotective effects. All sections stained with hematoxylin and eosin (H&E); magnification: 40×. Scale bar: 75 μm.

oxidative stress (Table 11 and Fig. 22). Baicalin administration significantly shifted this gradient, suggesting effective preservation of organ architecture and function, particularly in organs critical for metabolic and circulatory regulation.

5.5. Western blot analysis validates multitarget modulation by baicalin in heat-stressed organs

To experimentally validate the *in silico* predictions and histopathological outcomes, Western blotting was conducted to quantify the expression of key stress-responsive and metabolic proteins—Hsp70, Hsp27, IL-6R, and CYP3A4—in organ-specific lysates from the control, hyperthermia, and baicalin + hyperthermia groups. GAPDH was used as the internal loading control to ensure uniform protein normalization across tissues. Preliminary validation confirmed consistent GAPDH expression across brain, heart, liver, kidney, and lung samples, supporting its reliability as a reference control. However, future experiments will include β-actin as an additional loading reference to further confirm normalization consistency.

As illustrated in Fig. 23, hyperthermia markedly upregulated Hsp70 in the brain and Hsp27 in the heart, reflecting activation of cellular stress responses and cytoskeletal destabilization ($p < 0.05$). IL-6R levels were significantly elevated in lung tissue, consistent with thermal stress–induced inflammatory signaling, while hepatic CYP3A4 expression was substantially suppressed, indicating impaired xenobiotic metabolism and hepatocellular stress.

Baicalin pre-treatment effectively attenuated the hyperthermia-induced overexpression of Hsp70, Hsp27, and IL-6R, while restoring CYP3A4 expression toward baseline levels. These effects were corroborated by densitometric quantification, where normalized relative protein intensities confirmed statistically significant modulation ($p < 0.05$).

Although kidney tissue was comprehensively analyzed histopathologically, protein-level validation was not performed due to limited sample yield from the same cohort. This

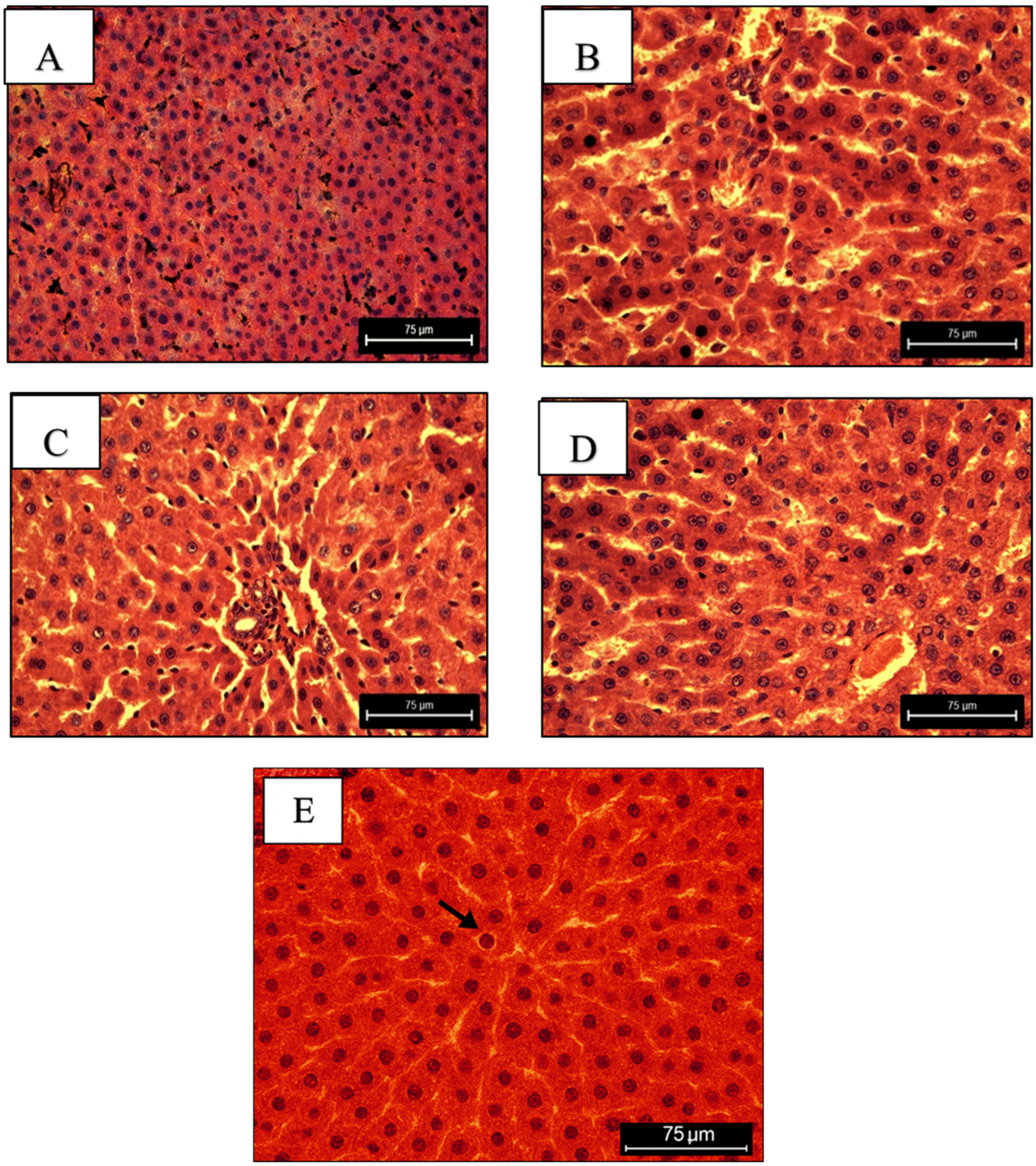

Fig. 19 Histopathological examination of liver tissue in Wistar rats subjected to hyperthermic stress and baicalin treatment. Representative hematoxylin and eosin (H&E)–stained liver sections demonstrating structural and inflammatory alterations induced by heat stress and the restorative effects of baicalin. (A) Control liver showing well-organized hepatic cords radiating from central veins with intact sinusoidal architecture. (B) Hyperthermia-exposed section revealing Kupffer cell activation, characterized by hypertrophic, rounded macrophages (arrow), indicative of heightened inflammatory response. (C) Bile duct hyperplasia (arrow), reflecting cholangiocyte proliferation secondary to inflammatory stress. (D) Marked sinusoidal and portal vascular congestion (arrow) with evident capillary dilation, signifying hepatic circulatory impairment and microvascular stress. (E) Baicalin-treated liver displaying largely preserved lobular organization with mild hepatocellular vacuolation (arrow), reduced Kupffer cell activity, and restored sinusoidal integrity, confirming baicalin's hepatoprotective potential under thermal stress conditions. All sections were stained with H&E, visualized at 40× magnification, and include a scale bar of 75 µm.

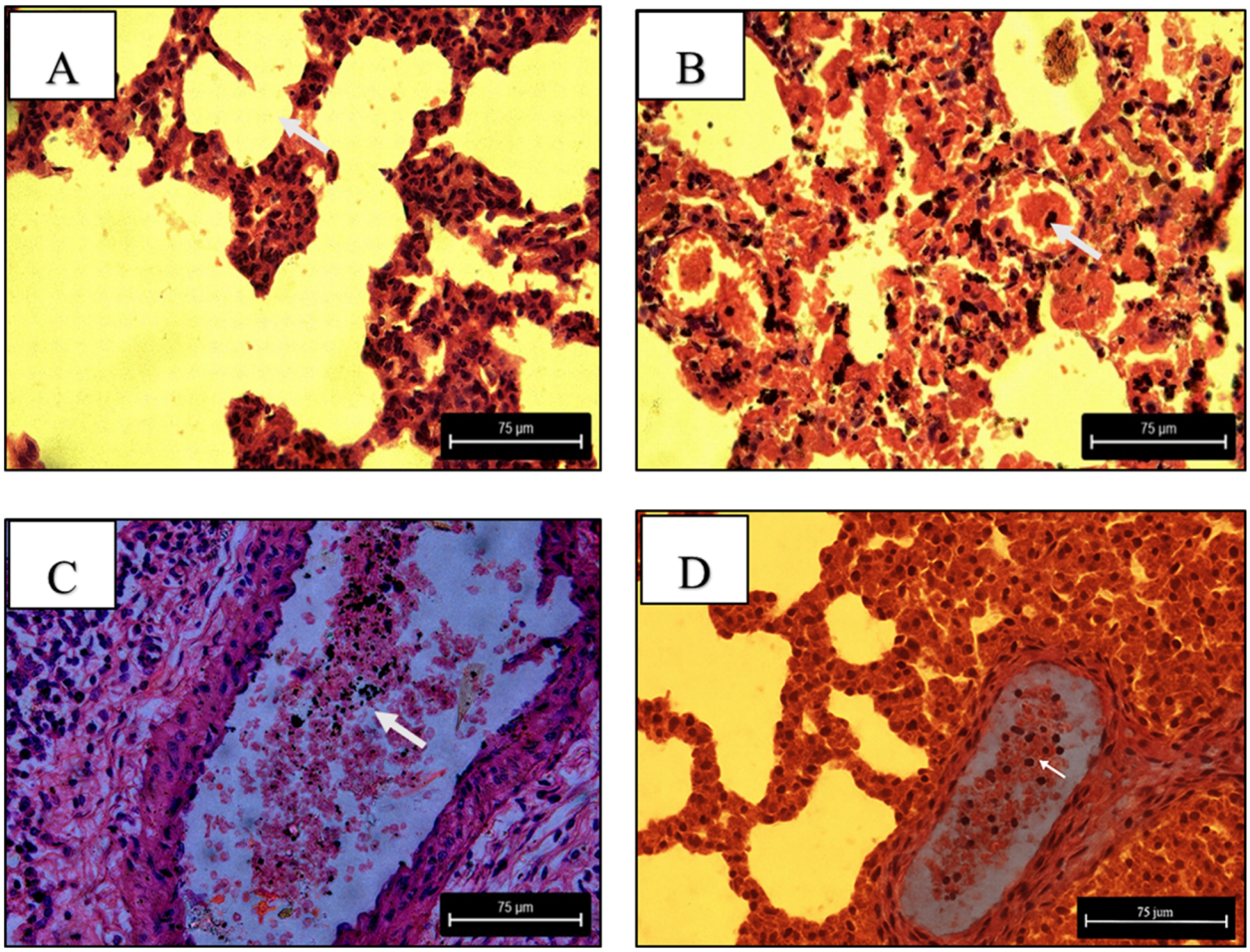

Fig. 20 Histopathological assessment of lung tissue in Wistar rats subjected to hyperthermic stress and baicalin treatment. Representative hematoxylin and eosin (H&E)–stained lung sections illustrating structural and inflammatory alterations induced by heat stress and the mitigating effects of baicalin. (A) Focal emphysematous changes in alveolar sacs (arrow), denoting alveolar wall destruction and airspace enlargement associated with oxidative and thermal damage. (B) Prominent vascular congestion within pulmonary capillaries (arrow), indicative of compromised microcirculatory function and early pulmonary edema. (C) Section showing bronchopneumonic infiltration, with dense mononuclear inflammatory cells occupying the bronchiolar lumen (arrow), consistent with an acute inflammatory response. (D) Baicalin-treated lung exhibiting marked reduction in inflammatory infiltration and partial restoration of alveolar integrity, though mild emphysematous changes and vascular congestion persist (arrows), demonstrating moderate pulmonary protection and attenuation of heat-induced injury. All sections were stained with H&E, visualized at 40× magnification, and include a scale bar of 75 μm.

omission is recognized as a study limitation and will be addressed in future experiments through inclusion of renal-specific markers and protein expression analyses.

Collectively, these findings corroborate the multitarget interactions and dynamic stability predicted computationally, providing molecular-level evidence that baicalin confers broad-spectrum cytoprotection under systemic hyperthermic stress. While the results confirm functional modulation rather than direct binding, they substantiate baicalin's capacity to regulate key stress, inflammatory, and metabolic pathways, reinforcing

Table 10 Semi-quantitative scoring of organ-specific histopathological alterations

Organ	Lesion type	Control	Hyperthermia control	Baicalin treated
Brain	Gliosis, neuronophagia	0	2	1
Heart	Congestion, hemorrhage, myocyte degeneration	0	3	1
Kidney	Tubular injury, vacuolar degeneration	0	3	1–2
Liver	Sinusoidal congestion, Kupffer activation	0	3	1
Lung	Emphysema, pneumonia, inflammation	0	3	2

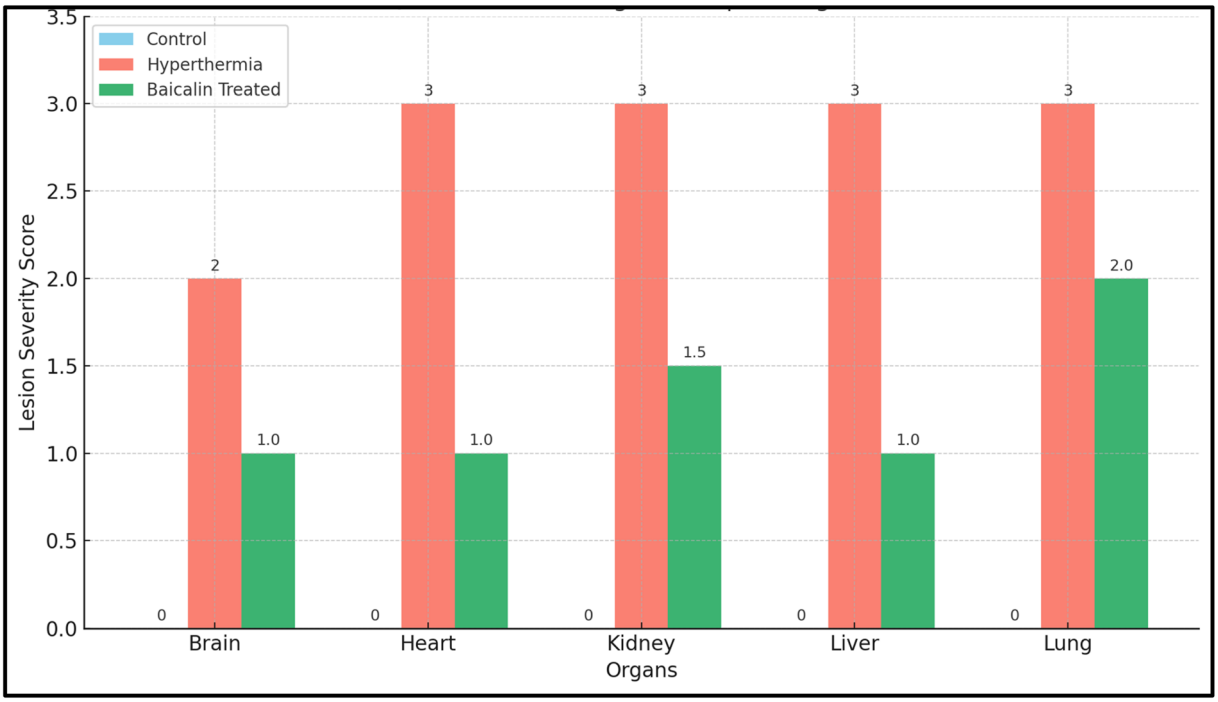

Fig. 21 Semi-quantitative scoring of histopathological lesions across major organs in control, hyperthermia-exposed, and baicalin-treated groups. Bar chart representing mean lesion severity scores (0 = none, 1 = mild, 2 = moderate, 3 = severe) for brain, heart, liver, kidney, and lung tissues. Hyperthermia exposure resulted in marked histopathological alterations across all organs, with the lungs exhibiting the highest lesion severity, followed by the liver and kidney. Baicalin pre-treatment significantly attenuated tissue injury, reflected by notably reduced lesion scores in all examined organs. These results demonstrate baicalin's broad-spectrum cytoprotective efficacy and its ability to ameliorate heat-induced multi-organ damage. Data expressed as mean ± SEM ($n = 6$); statistical significance determined by one-way ANOVA followed by Tukey's post hoc test ($p < 0.05$ *vs.* hyperthermia group).

Table 11 Summary of observed histopathological features across groups[a]

Organ	Control group findings	Hyperthermia group findings	Baicalin-treated group findings
Brain	Normal neurons, no gliosis	Neuronophagia, gliosis	Mild gliosis, intact neurons
Heart	Normal striations	Hemorrhage, vascular congestion	Mild myocyte degeneration
Kidney	Normal tubules and glomeruli	Tubular necrosis, cloudy swelling	Partial recovery of tubules
Liver	Healthy hepatic cords	Kupffer cell activation, congestion	Reduced Kupffer reactivity
Lung	Intact alveoli	Pneumonia, emphysema	Decreased infiltration

[a] Computational modeling suggested multitarget interaction, while *in vivo* validation confirmed organ-specific protection in brain, heart, liver, kidney, and lungs under heat stress.

its promise as a natural pharmacological candidate for mitigating heat-induced multiorgan dysfunction.

The integrative pharmacoinformatics–experimental framework employed in this study revealed a coherent mechanistic alignment between computational predictions and *in vivo* outcomes. The observed modulation of stress-associated proteins (Hsp70, Hsp27, IL-6R, and CYP3A4) validates the predicted interaction profiles derived from molecular docking, MM-GBSA, and long-timescale MD simulations. These findings support baicalin's multitarget adaptability, enabling concurrent attenuation of thermal stress, inflammatory signaling, and metabolic disruption across multiple organ systems.

Although the present results strongly support baicalin's role as a multifunctional cytoprotective molecule, they do not directly confirm ligand–protein binding. Future work incorporating surface plasmon resonance (SPR) or isothermal titration calorimetry (ITC) could provide definitive kinetic and thermodynamic validation of these interactions.

5.5.1 Limitations of the study. This study's limitations include the absence of direct biochemical confirmation of baicalin–protein binding (*e.g.*, SPR or ITC) and the lack of pharmacokinetic quantification of baicalin distribution across organs. Future work will employ surface plasmon resonance assays and LC-MS-based biodistribution analyses to validate

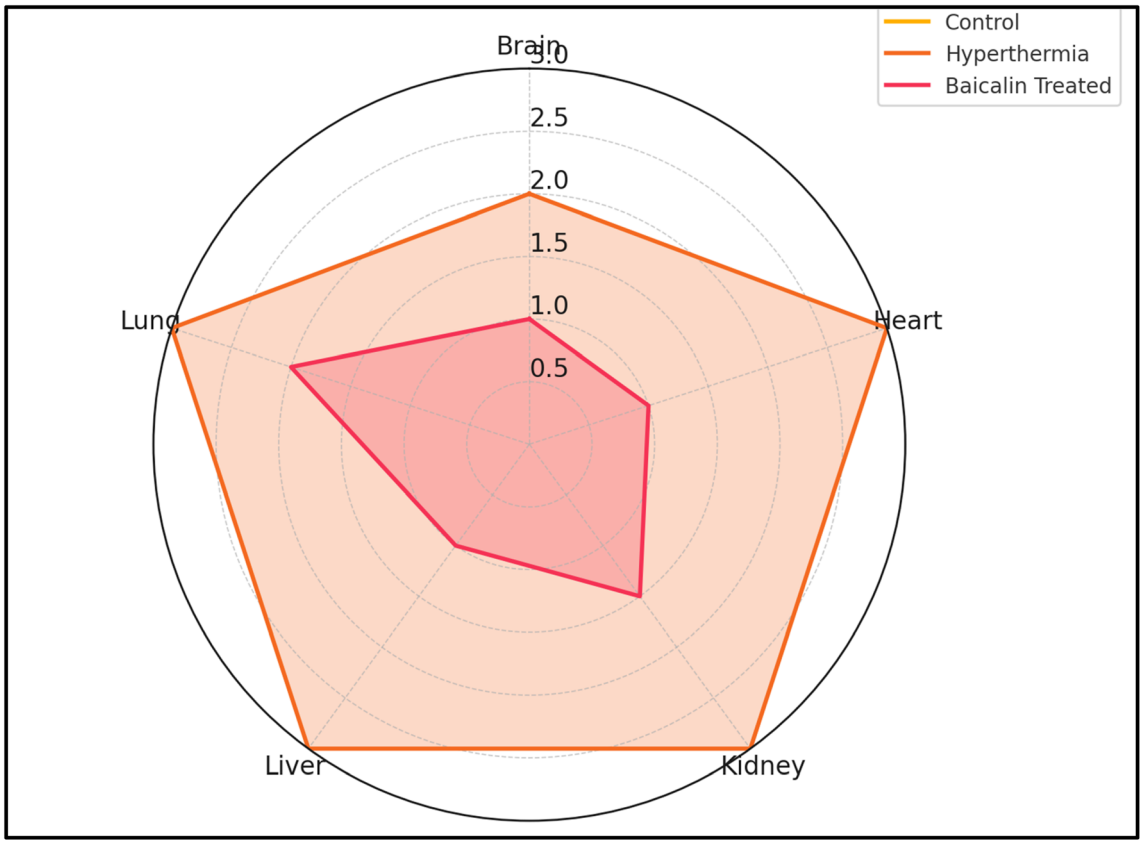

Fig. 22 Radar chart comparing lesion severity scores across five major organs in control, hyperthermia-exposed, and baicalin-treated groups. Radar plot illustrating the comparative distribution of semi-quantitative lesion scores for the brain, heart, liver, kidney, and lungs under different treatment conditions. The hyperthermia group displays a markedly expanded polygon, reflecting high pathological burden and extensive tissue injury across all organs. In contrast, the baicalin-treated group exhibits a contracted profile, indicating substantial reduction in lesion severity and multiorgan protection. The control group forms a compact baseline polygon, consistent with normal histoarchitecture and absence of pathological lesions.

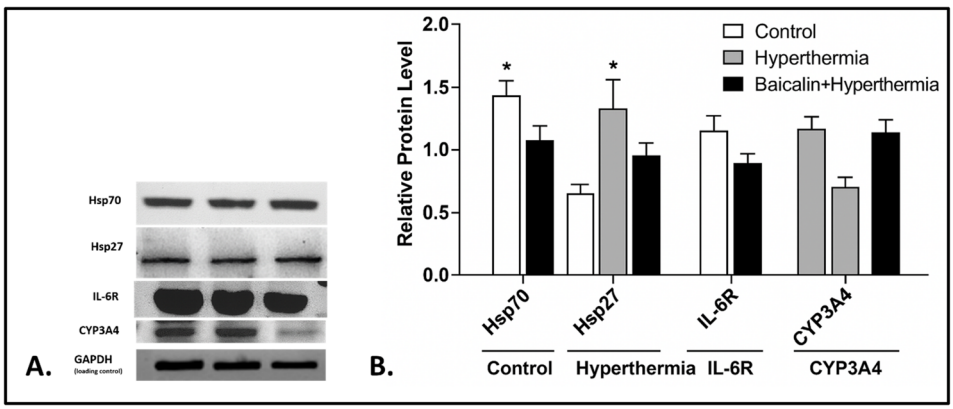

Fig. 23 Western blot analysis and densitometric quantification of heat stress–associated proteins in control, hyperthermia-exposed, and baicalin-treated rats. (A) Representative Western blots (right) and corresponding densitometric analyses (left) showing expression profiles of Hsp70 (brain), Hsp27 (heart), IL-6R (lung), and CYP3A4 (liver) across experimental groups: control (lane 1), hyperthermia (lane 2), and baicalin + hyperthermia (lane 3). GAPDH served as the internal loading control. (B) Quantitative analysis revealed that hyperthermia markedly upregulated Hsp70, Hsp27, and IL-6R expression ($p < 0.05$), while CYP3A4 was significantly downregulated. Baicalin pre-treatment effectively normalized protein expression, attenuating heat-induced overexpression of Hsp70, Hsp27, and IL-6R, and restoring CYP3A4 to near-control levels. Data are presented as mean ± SEM ($n = 3$); statistical significance determined by one-way ANOVA followed by Tukey's post hoc test ($p < 0.05$ *vs.* hyperthermia group).

these mechanistic interactions and optimize translational dosing.

6. Conclusion

This study provides comprehensive evidence that baicalin acts as a potent multitarget cytoprotective agent against acute systemic hyperthermia, validated through an integrated *in silico–in vivo* approach. Computational analyses identified five key heat-responsive proteins—Hsp70, Hsp27, aquaporin-1, IL-6R, and CYP3A4—as molecular targets, with baicalin demonstrating strong binding affinities ($\Delta G = -9.3$ to -8.5 kcal mol^{-1}), favorable thermodynamic stability (MM-GBSA $= -52.4$ to -68.7 kcal mol^{-1}), and highly stable conformations during extended molecular dynamics simulations (2000 ns; RMSD = 0.18–0.24 nm). Complementary DFT, dynamic cross-correlation, and free energy landscape analyses supported baicalin's electronic reactivity and conformational resilience across multiple protein environments, reinforcing its multitarget interaction potential.

In vivo evaluation in a rat whole-body hyperthermia model further confirmed baicalin's multiorgan protective efficacy, significantly reducing histopathological damage in the brain, heart, liver, kidney, and lungs. Semi-quantitative scoring demonstrated a marked decline in lesion severity (notably from score 3 → 1 in hepatic and cardiac tissues), while western blot assays revealed normalization of heat-induced dysregulation—downregulation of Hsp70, Hsp27, and IL-6R, alongside restoration of CYP3A4 expression. These findings highlight baicalin's ability to simultaneously modulate stress, inflammatory, and metabolic pathways at the protein level.

In silico ADMET and ProTox-II analyses indicated a favorable safety profile ($LD_{50} \approx 5000$ mg kg^{-1}; non-mutagenic; non-hepatotoxic), though limited gastrointestinal absorption suggests the need for formulation refinement to improve systemic bioavailability.

Collectively, this work not only underscores baicalin's therapeutic promise as a natural multitarget cytoprotective agent but also exemplifies how integrative pharmacoinformatics–experimental frameworks can accelerate discovery of effective interventions against stress-induced multiorgan dysfunction. Future studies incorporating direct biophysical binding assays and pharmacokinetic validation will further strengthen the mechanistic understanding and translational potential of baicalin in heat-related systemic disorders.

Author contributions

Anjali Kumari: *in vivo* experiments, investigation, conceptualized, writing the original draft (*in vivo* experimental part), validation, data curation, validation and Formal analysis. Aisha Tufail: writing the original draft (molecular docking), visualization, validation. Magda H. Abdellattif: formal analysis and validation of western blot and *in vivo* studies. Amit Dubey: supervision (computational), investigation, conceptualized, writing the original draft, software (molecular docking, molecular dynamics simulations, PCA, DCCM, DFT, MESP, and ADMET), visualization, methodology, writing – review & editing, data curation, validation and formal analysis. Rakesh Kumar Sinha: supervision (*in vivo* experimental part), investigation, conceptualized, writing – review & editing (*in vivo* experimental part), data curation, validation and formal analysis.

Conflicts of interest

All the authors declared no conflict of interests.

Data availability

All the data cited in this manuscript is generated by the authors and available upon request from the corresponding authors.

Supplementary information is available. See DOI: https://doi.org/10.1039/d5ra05510e.

Acknowledgements

Authors sincerely thank and acknowledge Ahmad Hussain for his support during the histopathology experiment, and Birla Institute of Technology, Mesra, Ranchi Jharkhand (India) for providing lab facilities. The authors extend their appreciation to Taif University, Saudi Arabia for supporting this work through project number TU-DSPP-2024-19.

References

1 C. P. Chang, W. T. Huang, B. C. Cheng, C. C. Hsu and M. T. Lin, The flavonoid baicalin protects against cerebrovascular dysfunction and brain inflammation in experimental heatstroke, *Neuropharmacology*, 2007, **52**(3), 1024–1033, DOI: 10.1016/j.neuropharm.2006.10.018.

2 H. Li, X. Cong, W. Yu, Z. Jiang, K. Fu, R. Cao, W. Tian and Y. Feng, Baicalin inhibits oxidative injures of mouse uterine tissue induced by acute heat stress through activating the Keap1/Nrf2 signaling pathway, *Res. Vet. Sci.*, 2022, **152**, 717–725, DOI: 10.1016/j.rvsc.2022.10.005.

3 J. Li, Y. Liu, J. He and W. Yao, Baicalin ameliorates heat stress-induced hepatic injury and intestinal microecology dysbiosis in late gestational mice, *Ecotoxicol. Environ. Saf.*, 2024, **283**, 116832, DOI: 10.1016/j.ecoenv.2024.116832.

4 P. Baindara, A. Jana, R. Dinata and S. M. Mandal, Heatstroke-Induced Inflammatory Response and Therapeutic Biomarkers, *Biomedicines*, 2025, **13**(2), 261, DOI: 10.3390/biomedicines13020261.

5 T. Y. Kao, C. C. Chio and M. T. Lin, Hypothalamic dopamine release and local cerebral blood flow during onset of heatstroke in rats, *Stroke*, 1994, **25**(12), 2483–2486, DOI: 10.1161/01.str.25.12.2483.

6 S. Song, L. Ding, G. Liu, T. Chen, M. Zhao, X. Li, M. Li, H. Qi, J. Chen, Z. Wang, Y. Wang, J. Ma, Q. Wang, X. Li and Z. Wang, The protective effects of baicalin for respiratory diseases: an update and future perspectives, *Front. Pharmacol*, 2023, **14**, 1129817, DOI: 10.3389/fphar.2023.1129817.

7 S. A. Zakki, Z. G. Cui, L. Sun, Q. W. Feng, M. L. Li and H. Inadera, Baicalin Augments Hyperthermia-Induced Apoptosis in U937 Cells and Modulates the MAPK Pathway via ROS Generation, *Cell. Physiol. Biochem.*, 2018, **45**(6), 2444–2460, DOI: 10.1159/000488263.

8 X. Li, F. Xv, L. Z. Ma, L. Xing, J. B. Zhao, W. J. Zhi, L. F. Wang, Y. Wang, H. D. Mao, S. Y. Liu, Y. H. Liu and Q. Song, Acquired heat acclimation in rats subjected to physical exercise under environmental heat stress alleviates brain injury caused by exertional heat stroke, *Brain Res.*, 2023, **1811**, 148393, DOI: 10.1016/j.brainres.2023.148393.

9 D. Hao, Y. Li, J. Shi and J. Jiang, Baicalin alleviates chronic obstructive pulmonary disease through regulation of HSP72-mediated JNK pathway, *Mol Med*, 2021, **27**(1), 53, DOI: 10.1186/s10020-021-00309-z.

10 S. J. Kim, Y. J. Moon and S. M. Lee, Protective effects of baicalin against ischemia/reperfusion injury in rat liver, *J. Nat. Prod.*, 2010, **73**(12), 2003–2008, DOI: 10.1021/np100389z.

11 M. Z. Khan, L. Li, Y. Zhan, H. Binjiang, X. Liu, X. Kou, A. Khan, A. Qadeer, Q. Ullah, K. J. Alzahrani, T. Wang, C. Wang and M. Zahoor, Targeting Nrf2/KEAP1 signaling pathway using bioactive compounds to combat mastitis, *Front Immunol*, 2025, **16**, 1425901, DOI: 10.3389/fimmu.2025.1425901.

12 R. Díaz, J. W. Kim, J. J. Hui, Z. Li, G. P. Swain and K. S. K. Fong, Evidence for the epithelial to mesenchymal transition in biliary atresia fibrosis, *Hum. Pathol.*, 2008, **39**, 102–115, DOI: 10.1016/j.humpath.2007.05.021.

13 RCSB Protein Data Bank. https://www.rcsb.org accessed May 2025.

14 UniProt: The Universal Protein Resource. https://www.uniprot.org accessed May 2025.

15 S. Kim, *et al.*, PubChem 2023 update, *Nucleic Acids Res.*, 2023, **51**(D1), D1373–D1380, DOI: 10.1093/nar/gkac956.

16 N. Guex and M. C. Peitsch, Swiss-PdbViewer: A Fast and Easy-to-Use Program for Protein Modeling, *Electrophoresis*, 1997, **18**, 2714–2723, DOI: 10.1002/elps.1150181505.

17 *Baicalin. PubChem CID: 64982*, https://pubchem.ncbi.nlm.nih.gov/compound/64982.

18 *Quercetin. PubChem CID: 5280343*, https://pubchem.ncbi.nlm.nih.gov/compound/5280343.

19 *Curcumin. PubChem CID: 969516*, https://pubchem.ncbi.nlm.nih.gov/compound/969516.

20 *Resveratrol. PubChem CID: 445154*, https://pubchem.ncbi.nlm.nih.gov/compound/445154.

21 *Apigenin. PubChem CID: 5280443*, https://pubchem.ncbi.nlm.nih.gov/compound/5280443.

22 M. D. Hanwell, *et al.*, Avogadro: An advanced semantic chemical editor, visualization, and analysis platform, *J. Cheminform.*, 2012, **4**, 17, DOI: 10.1186/1758-2946-4-17.

23 O. Trott and A. J. Olson, AutoDock Vina: Improving the speed and accuracy of docking with a new scoring function, efficient optimization and multithreading, *J. Comput. Chem.*, 2010, **31**, 455–461, DOI: 10.1002/jcc.21334.

24 R. A. Laskowski and M. B. Swindells, LigPlot+: Multiple ligand–protein interaction diagrams for drug discovery, *J. Chem. Inf. Model.*, 2011, **51**(10), 2778–2786, DOI: 10.1021/ci200227u.

25 M. J. Abraham, *et al.*, GROMACS: High performance molecular simulations through multi-level parallelism from laptops to supercomputers, *SoftwareX*, 2015, **1–2**, 19–25, DOI: 10.1016/j.softx.2015.06.001.

26 R. Kumari, R. Kumar and A. Lynn, g_mmpbsa—A GROMACS Tool for High-Throughput MM-PBSA Calculations, *J. Chem. Inf. Model.*, 2014, **54**(7), 1951–1962, DOI: 10.1021/ci500020m.

27 A. Amadei, A. B. M. Linssen and H. J. C. Berendsen, Essential dynamics of proteins, *Proteins Struct. Funct. Genet.*, 1993, **17**, 412–425, DOI: 10.1002/prot.340170408.

28 B. J. Grant, *et al.*, Bio3D: An R package for the comparative analysis of protein structures, *Bioinformatics*, 2006, **22**(21), 2695–2696, DOI: 10.1093/bioinformatics/btl461.

29 M. J. Frisch *et al. Gaussian 16, Revision C.01*, Gaussian, Inc., Wallingford CT, 2016.

30 A. Daina, O. Michielin and V. Zoete, SwissADME: A free web tool to evaluate pharmacokinetics, drug-likeness and medicinal chemistry friendliness of small molecules, *Sci. Rep.*, 2017, **7**, 42717, DOI: 10.1038/srep42717.

31 D. E. V. Pires, T. L. Blundell and D. B. Ascher, pkCSM: Predicting small-molecule pharmacokinetic and toxicity properties using graph-based signatures, *J. Med. Chem.*, 2015, **58**(9), 4066–4072, DOI: 10.1021/acs.jmedchem.5b00104.

32 P. Banerjee, *et al.*, ProTox-II: A webserver for the prediction of toxicity of chemicals, *Nucleic Acids Res.*, 2018, **46**(W1), W257–W263, DOI: 10.1093/nar/gky318.